2011

DESIGN, TESTING, AND ANALYSIS OF A NOVEL FATIGUE TESTING APPARATUS

Michael Falco
University of Rhode Island, mfalco27@gmail.com

DESIGN, TESTING, AND ANALYSIS OF A NOVEL FATIGUE TESTING APPARATUS

BY

MICHAEL FALCO

A THESIS SUBMITTED IN PARTIAL FULFILLMENT OF THE

REQUIREMENTS FOR THE DEGREE OF

MASTERS OF SCIENCE

IN

MECHANICAL ENGINEERING AND APPLIED MECHANICS

UNIVERSITY OF RHODE ISLAND

2011

MASTER OF SCIENCE THESIS

OF

MICHAEL FALCO

APPROVED:

Thesis Committee:

Major Professor Dr. David Chelidze

Dr. Philip Datseris

Dr. George Tsiatas

Nasser H. Zawia
DEAN OF THE GRADUATE SCHOOL

UNIVERSITY OF RHODE ISLAND
2011

ABSTRACT

A novel fatigue testing apparatus, its design, testing, and dynamical characterization are described. The apparatus, capable of high frequencies, loads the specimen with inertial forces of arbitrary load history. A sensing system is incorporated to allow for the study of the coupling between fatigue crack evolution and system dynamics. A numerical model of the system is described and its parameters are estimated using nonlinear system identification tools.

Testing of the system reveals its capabilities, advantages and disadvantages. Descriptions of modifications to the system are given, and the apparatus is evaluated as a successful platform for the study of the interplay between fatigue and system dynamics.

Fatigue experiments at different amplitudes are conducted, and the methods of *phase space warping* (PSW) and *smooth orthogonal decomposition* (SOD) are used in order to track the slowly drifting crack growth within the fast-time system dynamics. The capabilities of the algorithms are shown for randomly and chaotically excited systems. The rainflow counting method is applied in conjunction with the Palmgren-Miner linear damage law to investigate the effects of time history on fatigue accumulation. Testing results show that linear damage laws are not good models for prediction of fatigue failure and time to failure is largely based on time history. These conclusions are motivation for the further study of a predictive fatigue model which does not rely on microscopic *a priori* information such as initial crack length or micro-crack distribution.

ACKNOWLEDGEMENTS

First I would like to thank my friends and family who have been supportive of my academic endeavors.

I would like to take the time to express my gratitude to all of the people, who have been involved in my studies at URI, especially my thesis committee members Dr. David Chelidze, Dr. Philip Datseris, Dr. George Tsiatas, and Dr. Mayrai Gindy. The guidance and direction of my advisor Dr. David Chelidze has been invaluable to my educational experience at URI. I would like to particularly thank Professor Ming Liu, from whom I learned an enormous amount of technical and practical skills, along with my other lab mates Dr. David Segala and Nguyen Hai Son who have been tremendously supportive and helpful. I also would like to thank all the faculty and staff in the Mechanical Industrial and Systems Engineering department, especially Dave Ferreira, Jen Cerullo, Joe Gomez, and Jim Byrnes who have always been willing to help.

TABLE OF CONTENTS

LIST OF TABLES

LIST OF FIGURES

CHAPTER 1

INTRODUCTION

Material fatigue has been a long standing topic of interest, and the question of "why things break" has been addressed by many researchers in multiple disciplines of engineering. Fatigue is studied to understand how and or when a structural element will fail. Historically, tragic incidents such as the Versailles rail accident and the Comet aircraft crash (1842 and 1945 respectively) have compelled researchers to study fatigue (Smith & Hillmansen, 2004). Regardless of the efforts of countless researchers events such as the August 1, 2007 collapse of the I-35W bridge located in Minneapolis, Minnesota remind us that fatigue failures can still prove catastrophic today.

Advances in solid mechanics have been made and various fatigue models based on linear damage rules and crack growth models are available (Fatemi & Yang, 1998). The study of linear elastic fracture mechanics has provided us with the Paris Law (Sanford, 2003), and experimental studies have given us design criteria in the form of the Palmgren-Miner Rule (Budynas & Nisbett, 2008). Both are used and accepted within the scientific and industrial communities. However, these methods require very specific and difficult to obtain *a priori* knowledge about the component and initial states of damage, such as crack length or micro damage distribution.

The Palmgren-Miner rule is a very simple form of a cumulative fatigue damage model. It is a stress-based method which relies on the use of S-N curves. An S-N curve simply relates fatigue life in numbers of cycles, N, to an applied stress. The Palmgren-Miner rule assumes that damage is a cumulative sum described as $D = \sum_i n_i/N_i$ where n_i is the number of applied cycles and N_i is the total number of cycles to failure at the stress level σ_i (N_i is obtained from an S-N curve of the testing material). In other words, this rule states that the damage accumulated at each *i*-th stress level is cumulative and can be superimposed to calculate the total damage and is independent of the loading history. Variable loading is addressed with a combination of cycle counting, where variable load histories are broken into a number of constant load cycles, and the Palmgren-Miner rule. An example of this practice is a study on the fatigue life of steel girders on the Yangpu cable-stayed bridge (built in Shanghai, China) based on variable loading due to wind buffeting (Gu, Xu, Chen, & Xiang, 1999). This theory also ignores the presence of small stress cycles which lie below the fatigue limit, which may or may not affect the total fatigue damage.

The Paris Law is a fatigue crack propagation model which has been derived from linear elastic fracture mechanics. A classical form of the Paris equation [Paris 1961] is

$$\frac{da}{dN} = C(\Delta K)^m, \tag{1.1}$$

where $\Delta K = Y\sigma\sqrt{\pi a}$ is a stress intensity factor, a is crack length, C and m are material constants, and Y is a geometry factor. There exists a threshold value, K_{th}, below which crack propagation will not occur. This can be likened to the fatigue limit evident on a typical S-N curve. The downfall to this method is the requirement for

previous knowledge of initial crack length. This type of microscopic information is very hard and often impossible to obtain in real world applications. A second issue is the consideration of variable amplitude loading rather than cyclic amplitude loading. Unlike the Miner rule, Paris' equation does not discount the affects of loading history and this becomes a much more complicated problem. Methods such as the Wheeler model require cycle-by-cycle integration of crack growth which attempt to include the affects of over-stressing and are both very complicated and computationally expensive (Anderson, 1995).

There exists a need for the development of real time procedures, which will be a significant improvement on the outlined damage models, to perform structural health monitoring (SHM) and condition based maintenance (CBM) tasks. It is the aspiration of this research to design and build a platform which can be used to empirically investigate such a model which requires no *a priori* knowledge of microscopic crack information, and will decide the state of fatigue damage of a system. The platform is tailored to meet these research goals and includes several key features which will be outlined.

Variable amplitude loading is possible with current fatigue testing apparatuses (Sonsino, 2007) but they do not take into account the effects of inertial and damping forces within a system. Typical fatigue testing machines can be classified by methods of load application as spring forces or dead weights, centrifugal forces, hydraulic forces, pneumatic forces, thermal dilation forces, or electro-magnetic forces (Galal & Shawki, 1990). Systems made to study the effects of inertial loading are limited in existence and availability. The new fatigue apparatus designed and built for this study

is based on the fatigue testing apparatus designed by Wiereigroch's research group in Aberdeen, Scotland (Foong, Wiercigroch, & Deans, 2003). The capabilities of this system meet the requirements to achieve the research goals of the study. However the design has been streamlined for more efficient use and cost reduction.

There are two key features of the apparatus which are necessary for the study to be successful; the system does not ignore inertial forces, and any arbitrary type of loading can be applied (e.g., chaotic, random, and periodic). The ability to examine the interplay between system dynamics and fatigue crack growth is achieved by the mass-damper style loading employed in the system. Here, unlike available fatigue apparatuses, the fatiguing specimen is a crucial component of the system's structure. Therefore, the structural dynamics change drastically with the evolution of the fatigue crack.

The driving forces are provided by a programmable arbitrary function generator. Using this equipment any time series can be used for forcing input. In this study, time series are generated using Matlab (Mathworks, Natick, MA) and then converted to waveforms using Tektronix software (the details of this will be covered in the Methodology section).

An additional feature of the system is the ability to apply loading at any *R*-ratio which can be defined as $R = \sigma_{\min} / \sigma_{\max}$ where $\sigma_{\min}$ and $\sigma_{\max}$ are minimum and maximum stresses respectively. Also, the system is very adaptable to adding, removing or moving components as it is built on a slip table with evenly spaced mounting holes. This will also allow for the possibility of changing the geometry of

the specimen. The versatility of the data acquisition (DAQ) and sensing system allows various different measurements to be taken from the system which is useful for alternate test configurations. A final key feature of the testing apparatus is the ability to test at high frequencies. Currently tests are conducted in the 20-30 Hz range. Fast turnaround times in the design process require high-cycle fatigue testing to be done quickly, and this feature drastically reduces the time expenses necessary to run each experiment.

A reliable model of the healthy structure (the testing apparatus and a specimen with no fatigue crack) is necessary in order to investigate the dynamical interactions between fatigue crack evolution, load history, and structural dynamics. The model will describe the structural dynamics of the system, and serve as a baseline for further modeling efforts. This model is constructed using a three-step nonlinear system identification procedure. Standard modal analysis is only used to verify the employed methodologies because of the nonlinearity of the system.

Our predictive model will rely also on the ability to extract g*eneralized fatigue damage coordinates* (GFDC's) from the system dynamics data. These coordinates will describe the existing state of damage within the system and will be obtained using the methods of *phase space warping* (PSW) (Chelidze & Cusumano, 2006) and *smooth orthogonal decomposition* (SOD) (Chelidze & Zhou, 2008). These methodologies are used in conjunction to extract underlying slow-time processes using readily available fast-time measurements of a system. SOD is a multivariate, multiscale data analysis method that considers both spatial and temporal characteristics of the data. Particularly, SOD is used to find *smooth orthogonal*

coordinates (SOC's) which have minimal temporal roughness and maximal spatial variance over the feature vectors which are constructed by calculating some standard or common short-time statistical measure.

The method of PSW takes advantage of the small distortions in the phase space of the fast subsystem resulting from the slow parameter drift. The dynamical system of the following form is considered:

$$\dot{\boldsymbol{x}} = f(\boldsymbol{x}, \boldsymbol{\mu}(\phi), t), \tag{1.2}$$

$$\dot{\phi} = \varepsilon g(\boldsymbol{x}, \phi), \tag{1.3}$$

$$y = h(\boldsymbol{x}), \tag{1.4}$$

where $\boldsymbol{x} \in \mathbb{R}^m$ is the fast dynamic variable (observable state) $\phi \in \mathbb{R}^n$ is the hidden, underlying, slow dynamic variable, the parameter vector $\boldsymbol{\mu}$ is a function of $\boldsymbol{\phi}$, t is the time, the rate constant $0 < \varepsilon \ll 1$is defined as time-scale separation between the slow drift and fast time dynamics, and y is a scalar quantity observed under the smooth function $h(\boldsymbol{x})$.

In (Chelidze, Cusumano, & Chatterjee, 2002) this concept was applied to an electro-mechanical system where a cantilever beam oscillated between a permanent magnet and an electromagnet. In this study, the scalar time series y was collected from strain gauges mounted to the beam. The electromagnet was powered by a 9-volt battery and the slow time process, $\boldsymbol{\phi}$, represented the change in the potential field due to the slow discharge of the battery. Using the strain gauge data alone a PSW based

tracking metric was shown to have a one-to-one relationship with the depletion of the battery's voltage.

In (Chelidze & Liu, 2005), an experimental setup with a cantilevered beam oscillating between two permanent magnets is used. The setup is a well known experiment described and introduced in (Moon & Holmes, 1979). The system consists of a cantilevered beam, with a crack initiated near the cantilever, oscillating between two permanent magnets. The physics are simple enough for a model to be created, yet chaos can be observed within the system. Again strain gauge data is used to capture the fast time dynamics of the beam, and a tracking matrix, which is in relationship with the slow-time processes of the system, is extracted using PSW and SOD. The results show that the extracted slow time variable is in good accordance with the Paris Law as mentioned previously and represented by equation (1.1). Major additions of the work presented in this thesis, to the aforementioned work, are that there will be an independent measure of crack length, which can be compared to the extracted slow process and the system itself is more adaptable to various experimental designs.

The first main research objective was to establish a platform for the investigation of the interplay between structural dynamics and fatigue damage accumulation. Traditional fatigue tests ignore damping and inertial forces; however in practical real world situations fatigue accumulation is not isolated from these effects. In turn, fatigue accumulation will affect the parameters of the system altering the structural dynamics. Estimations of future loading patterns will be impossible without the knowledge of the relationship with fatigue and system dynamics. Accurate fatigue life estimations are impossible without the knowledge of all of these aspects.

A second goal of this research is to perform system identification of a healthy structure. A valid and accurate model of the system dynamics at a healthy state is necessary to begin to understand the effects of fatigue evolution. This will serve as the basis to any proposed modeling efforts.

The fact that many structures in real world applications are not subject to constant amplitude loadings provides the motivation to study variable load histories. It is currently understood that load factors are nonlinearly coupled with fatigue life. The Miner rule is inadequate in practice. It is the intention of this study to compare variable load fatigue life predictions with actual fatigue testing of specimens under variable loading conditions. Furthermore, chaotic loading is compared to random loading. Variable load history tests are conducted using a time series derived from the Duffing's equation and are compared to random tests which are derived using surrogate data techniques which preserve the power spectral density and the probability distribution function of the original chaotic time series (Schreiber & Schmitz, 1996), emphasizing the importance of time history in fatigue models. Cycle counting methods will be applied along with the Miner rule to investigate the predictive effectiveness of the technique. It is hypothesized that the resulting time to failures will not be comparable between the two types of testing. It is also hypothesized that simple cycle count based prediction will not reflect this phenomenon.

CHAPTER 2

METHODOLOGY

2.1 Mechanical System Design

The fatigue testing apparatus was carefully designed to incorporate the desirable features and reduce the cost as compared with the Wiereigroch research group's fatigue apparatus. A schematic of the novel apparatus is shown in Figure 1. The driving force of the mechanical system is a low force electromagnetic shaker (Ling Dynamic Systems, model V722) capable of a 2.9 kN peak force and supports up to a 100 kg payload. The maximum frequency of the shaker is about 4 kHz which is well above the design requirement. The backbone of the fatigue apparatus is a slip table guided by four linear bearings on two parallel rails mounted to a granite base. The granite base provides a sturdy foundation for the test setup. It is carefully aligned to be parallel with the axis of shaker in order to reduce any unnecessary wear on the shaker itself.

The slip table is constructed of a 25.4 mm thick aluminum plate with a 12.7 mm aluminum breadboard mounted above. The breadboard is pre-drilled and tapped for M6-1 bolts at regular spacing of 20 mm on center. This makes for a very adaptable mounting surface allowing for future modifications to the specimen or the system. The slip table is connected to and driven by the shaker. This connection is managed by a Nexen LK-2000 linear coupling. The coupling allows for angular misalignments

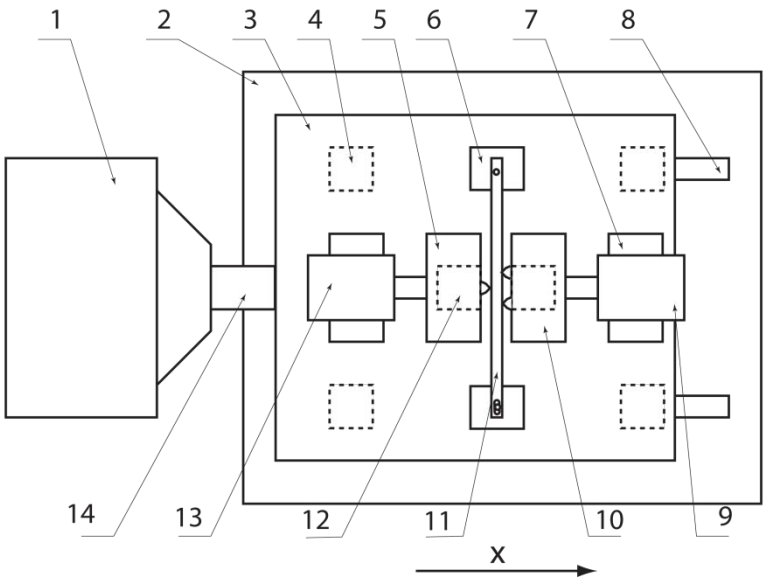

Figure 2 Schematic of the apparatus. 1. Shaker; 2. Granite base; 3. Slip table; 4.Linear bearing; 5. Back mass; 6. Specimen supports; 7. Pneumatic cylinder supports; 8. Rails; 9. Front cylinder; 10. Front mass; 11. The specimen; 12. Bearing blocks; 13. Back cylinder; 14. Flexible connector.

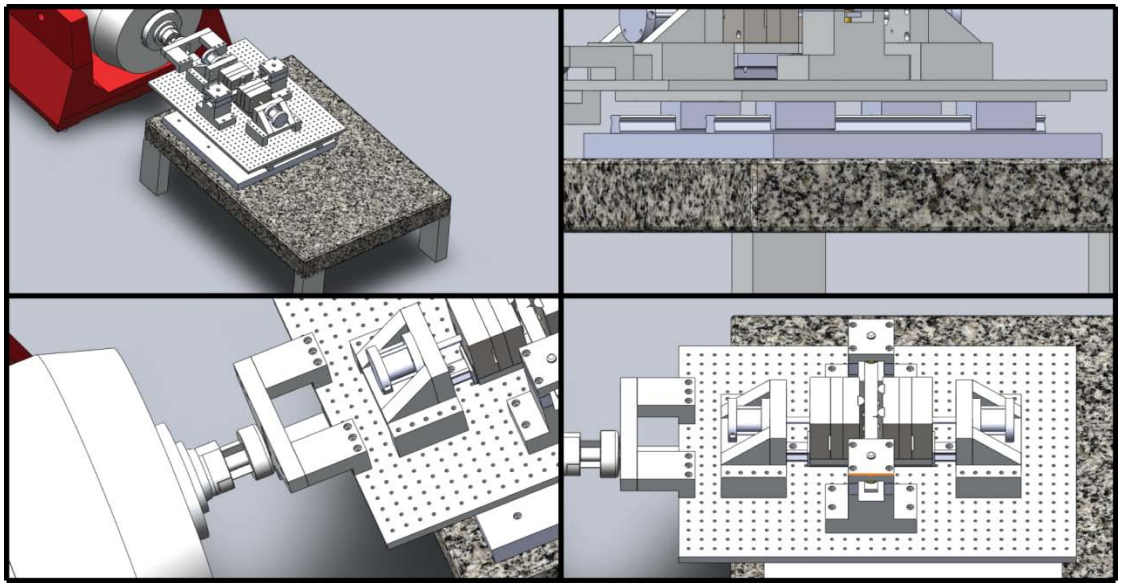

Figure 1 Model views of the apparatus. Top left: Granite base. Top right: Slip table mounted to linear bearings. Bottom Left: Zero axial backlash flexible coupling. Bottom Right: System components mounted to the slip table.

in all directions, but has zero axial backlash and can withstand forces up to 2000 N.

This coupling, combined with the careful alignment of the slip table and granite base,

should provide adequate protection to the internal bearings of the shaker.

The remainder of the apparatus is then constructed on top of the slip table. Two specimen support towers are mounted to the slip table. The specimen is a simply supported beam free to rotate about both pins and translate about one. The specimen, shown in close detail in Figure 3, has a round hole on one end and an oblong slot on the opposite end. It is crucial for contact between the specimen and the support pin to be maintained, while still meeting the simply supported condition. The support pins are made of steel tightly held to a tolerance of 12.7 mm. The hole of the specimen is machined to 12.700 mm and reamed to 12.725 mm providing a very tight fit between the pin and specimen. This is not a practical approach to maintain contact on the slot side of the specimen, and this issue will be addressed in a later portion of the design description.

The fatigue-inducing stresses are generated from the inertial masses (approximately 5.8 kg each). Each mass is mounted to a bearing block guided by linear rails. Two pneumatic cylinders are employed to keep the masses in constant contact with the specimen. The pneumatic cylinders are connected to a constant air supply and the pressure inside each cylinder is fully controllable by an air pressure regulator. Therefore, the stresses in the specimen can be altered by simply changing the pressure within the cylinders.

One obstacle in the design was the method of securing the beam in the vertical direction along the pin. In order to keep the condition of a simply supported beam, the ends of the specimen have to be free of clamping, but need to have a force keeping

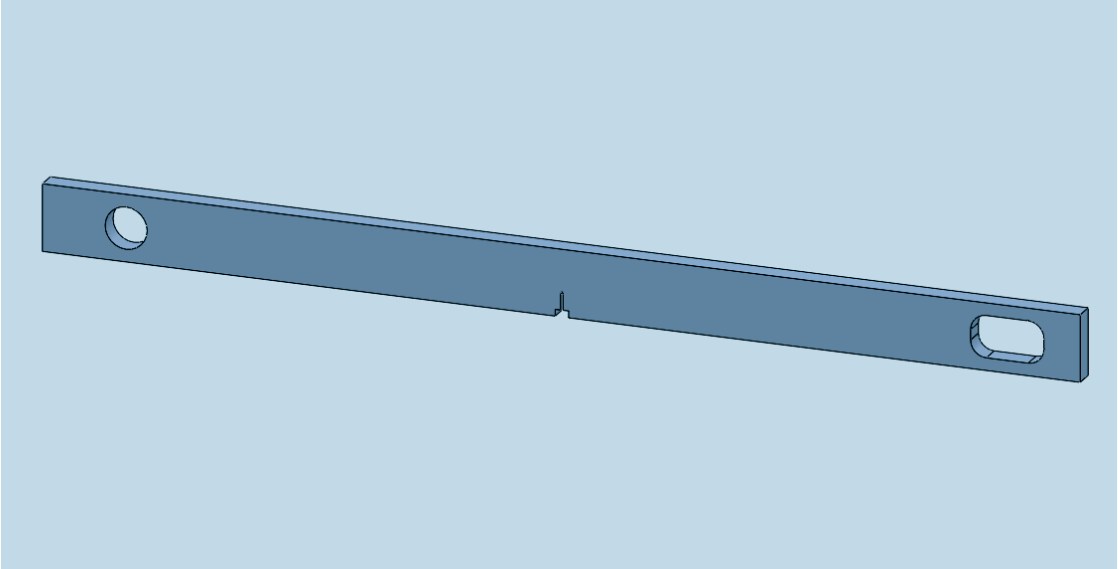

Figure 3. Solid model of the specimen. The machined notch can be seen in the center, the round hole on the left and the oblong slot on the right.

them from lifting. Initially the beam was held between two brass bushings which were in direct contact with the beam. This type of constraint required the tolerance on the specimen to be very tight in order to avoid modifications to the clamping structure. Audible clicking, indicative of under-clamping, coming from the specimen support area were observed on multiple occasions during initial testing. Also, over-clamping was evident in multiple tests. This was characterized by unusually long failure times and very long crack lengths. The solution to this problem was to modify the existing support system. Minimal changes were desired to avoid costly and time consuming re-machining. A simple, yet effective solution, shown in Figure 3, was to incorporate a spring in the design of the specimen support. A relatively stiff die spring was selected with a spring constant of 140 kN/m. The tolerance of the specimen material is ±0.203 mm. Therefore, with no adjustment the maximum change in force is only ±28.5 N. The spring is mounted along the support pin and between the specimen and

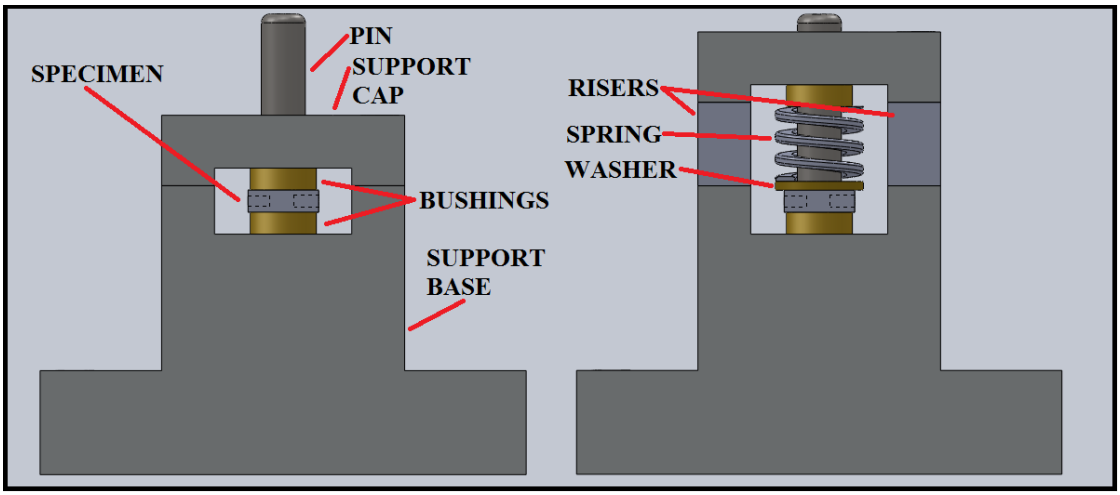

Figure 4. Solid model of the original support design (Left) and the modified support (Right).

the top bushing. A brass washer is included between the specimen and the spring in order to act as a bearing and maximize the contact area for an evenly applied spring force. The only components which needed to be machined were the two risers. Their proper height was determined by assembling the new setup without the risers, relying on the bolts and the spring force to keep the assembly together. The bolts were adjusted, increasing the compression on the spring, while the setup was also tested for freedom of rotation of the specimen about the pin. Once a proper height was established, the distance for the riser was measured. It should be noted that this new support structure was adapted on both support towers.

Another tolerance issue is the joint between the slot and the pin. It is manageable to hold a tight tolerance on a round hole, however the slot width varies slightly from specimen to specimen. If the slot is too tight it will not receive the pin and if the slot is too wide the play will cause constant collisions between the specimen and the pin. In order to eliminate this play while maintaining the condition that the beam is free to rotate and translate about the pin, a ball bearing set screw was added to the design.

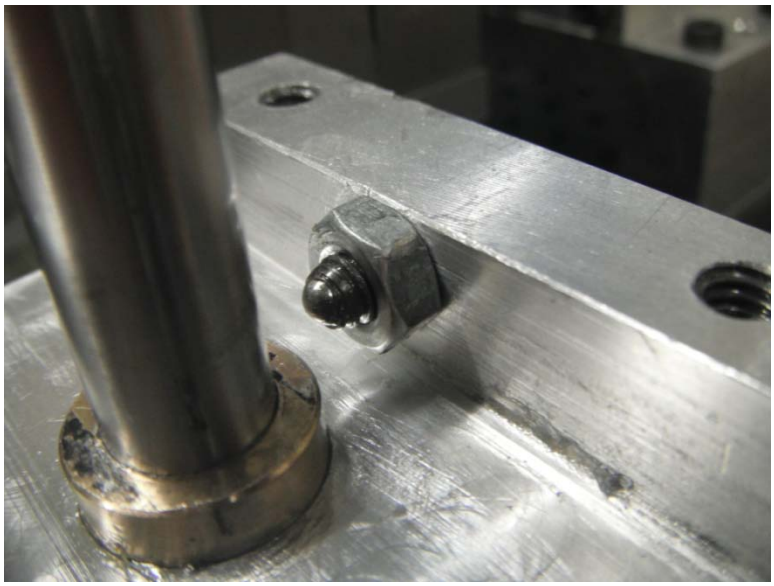

Figure 5. Photograph of the ball bearing set screw shown mounted in the support tower. Before testing begins the screw is tightened against the face of the specimen and the nut is tightened to resist loosening due to vibration.

The screw is a normal set screw with a steel roller ball mounted at its tip. A tapped hole was made at the correct height, in order for the center of the ball to contact the center of the specimen, through the slot side support base. This can be seen in the photograph provided (Figure 4). Before each experiment begins, the specimen is mounted and the set screw is tightened to make contact. Because the steel ball bearing is much harder than the aluminum the support tower can be unbolted and slid along the slot. This forms a shallow groove in the specimen in which the ball bearing is seated, with no play. The force from the screw keeps the specimen in constant contact with the pin while conserving all simply supported beam conditions.

2.2 Specimen Design and Preparation

The specimen is made of aluminum 6061-T6 bar stock with initial dimensions of 1828.80 mm × 25.40 mm × 6.35 mm ($l \times w \times t$). The final dimensions of each machined specimen are 314.71 mm × 20.32 mm × 6.35 mm. A drawing for the

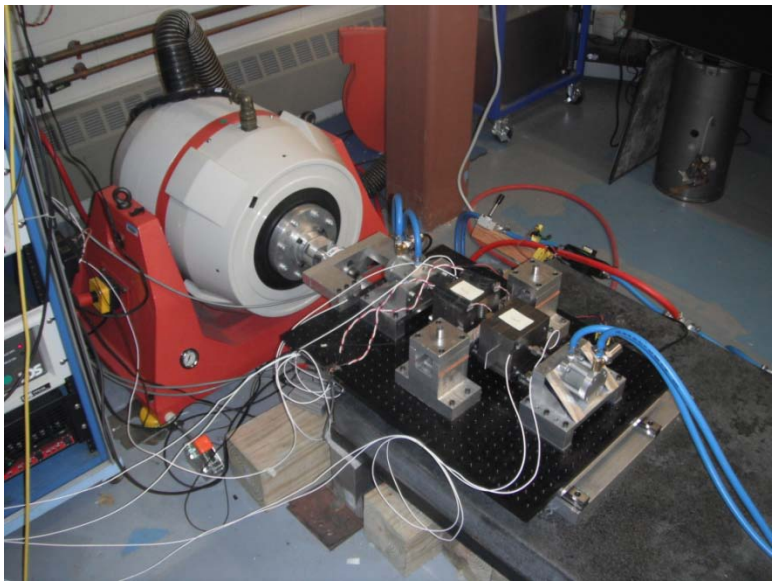

Figure 6. Photograph of the completed system.

specimen can be found in APPENDIX A. To initiate fatigue more easily and increase stress concentration in the beam, a V-notch is machined in the center of the specimen. The notch is cut to a depth of 7.62 mm by a blade 0.762 mm thick with a 60 degree V-shaped tip.

Since aluminum 6061 is heat treatable, the specimens are all fully annealed (reduced from T6 to T0) to remove stress from the manufacturing or machining processes, in order to keep the specimens as consistent as possible. The procedure for heat treating is relatively simple. The specimens are loaded into a heat treating oven, which is pre-heated to 775^{o} F and left to sit for a minimum of two hours. After which point the oven is shut off and the specimens are allowed to slowly cool. The rate of cooling must be lower than 50^{o} F per hour. This is easily achieved by the insulative properties of the oven.

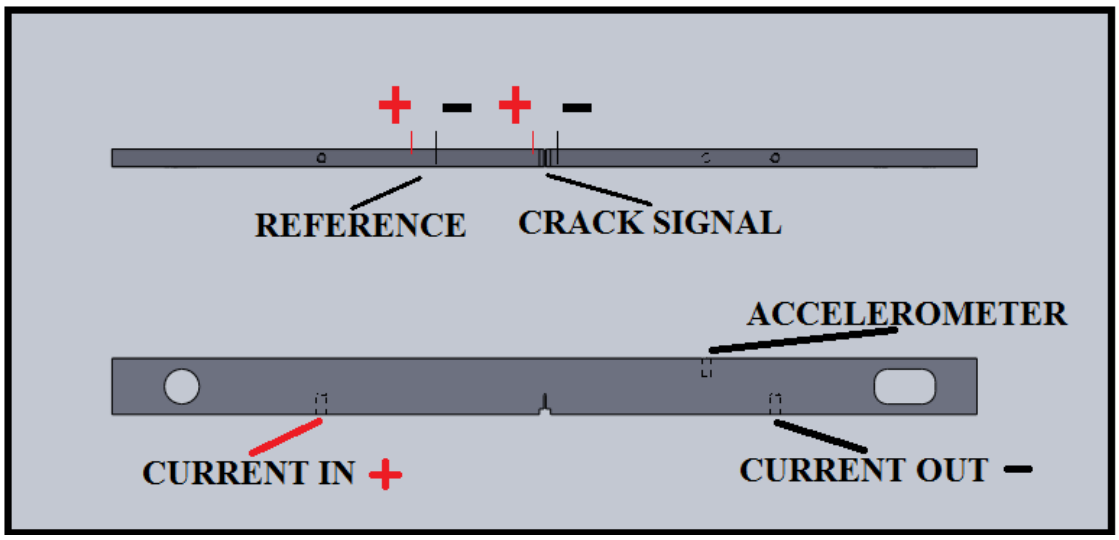

Figure 7. Solid model showing all electrical connections to the specimen. The polarity must be kept as shown. Also note the staggered positioning of the ACPD lead wires (top).

The hole and slot must be machined after annealing to avoid the issue of thermal expansion of the holes. Reaming a round hole is not a difficult task, but the slot is very difficult to open up if these are machined prior to annealing. The machining is done relatively far away from the crack tip and surrounding area so it is assumed there are no major stresses induced from this process.

The crack growth is monitored using an Alternating Current Potential Difference (ACPD) crack growth monitor. This system requires a current source connected to the specimen and two sets of leads to take measurements of the voltage drop for the reference and across the crack tip. The current source is connected via ring terminals which are mounted with two 6-32 machine screws directly into tapped holes on the front side of the specimen. The voltage leads are connected in a very precise manner according to the ACPD manufacturer by spot welding. A spot welded joint between aluminum and copper is not strong enough to withstand vibration testing

so the joint is reinforced using a two part epoxy which is specially formulated for high vibration situations. The connection between the lead and ACPD monitor is made using snap plug terminals which are isolated using *electro-magnetic interference* (EMI) shielding. An accelerometer is also mounted directly to the beam which simply requires one 5-40 tapped hole. The locations and orientations of all of these mounts can be seen in Figure 6.

When using the eddy current sensor to measure the displacement of the beam, it is necessary to mount, using double sided tape, a small aluminum plate to the specimen. It is required because the beam itself is too thin for the eddy current sensor to work properly. The dimensions of this plate are 25.400 mm × 12.700 mm × 3.175 mm.

2.3 Sensing/DAQ system

The system is monitored by a variety of sensors during each test and test set up including an eddy current sensor, piezoelectric accelerometers, pressure transducers, and load cells. Two single-axis accelerometers from PCB Piezoelectronics, model number 333B42, are used. A sensitive axis of each accelerometer is always kept parallel with the horizontal x-axis. These accelerometers are used to measure the dynamics of the system. Typical experimental configuration will use one accelerometer mounted to the rigid slip table and the other mounted to one of the two inertial masses. A third accelerometer also from PCB Piezoelectronics, model number 352C66, is mounted directly to the specimen via a tapped 5-40 hole. An eddy current displacement sensor from Lion Precision, model number U5 with driver number ECL202, is used to measure the displacement of one of the masses or the beam directly. These configurations will vary depending on the type of test being

conducted. Two PCB load cells are mounted in line between each mass and its associated pneumatic cylinder. These can be used to track the restoring force in the system. Two pressure transducers from PCB Piezoelectronics, model number 208C02, are mounted to the pneumatic cylinders. These are used during experimental setup to ensure accurate pressure levels in each cylinder. All data from the sensors are recorded at 1 kHz using a DAQ card from National Instruments connected to a PC and all control and DAQ tasks are implemented through a LabView program.

The drive signals for the shaker are generated by a Tektronix arbitrary function generator, model AFG 30222, which can produce standard output signals such as Gaussian noise and sinusoid. It also has the ability to output an arbitrary waveform which is programmed from any time series. The output signal is run through a low pass filter with cutoff frequency, set depending on the type of signal, in order to protect the system from high frequency components. The amplitude and frequency of the output signal can be controlled via a USB interface and the LabView environment. The signal is turned on and off (by a simple relay switch which uses the analog output capabilities of the DAQ card) when the system is ready to run and when the failure criteria has been met respectively. During a fatigue test the criteria for failure is reached when the specimen deforms to the point beyond the saturation of the eddy current sensor which measures the displacement of the beam. This feature is particularly useful for long time tests as no operator is required to monitor the system.

2.3 Testing Procedure

The experimental procedure is the same for all types of test run with only varying sensor locations or configurations of loading. The first step of any test is to prepare

the specimen. The voltage leads for the ACPD should be spot welded and epoxied prior to experimentation. At this point the current cables can be attached. It is very important to mount the cables with the correct polarity Figure 6. The positive current cable is mounted to the hole-side of the specimen and the negative cable is mounted to the slot side. This should be consistent with the polarity of the lead wires of the reference and signal measurements. The positive cable runs across the front edge of the specimen on the bottom face and is then secured using common tape in order to reduce signal variation due to movement of the cable. Both the current cables and voltage leads should be twisted around each other to reduce *electromagnetic interference* (EMI). Once the cables are mounted, and if the eddy current sensor is used to measure the displacement of the beam, the aluminum plate can be attached to the specimen in the proper location. The accelerometer must be screwed into its receiving hole and tightened securely. The beam can then be slid onto the pins, and the electrical connections to the sensing system can be made; the leads are connected using snap plug terminals and the current cables are connected using spade terminals.

All coincident surfaces between specimen and structure must be greased in order to reduce friction forces. Once the grease is applied, the ball bearing ball screw can be tightened up to the specimen and its lock nut can be tightened. The washer and spring can be stacked and the risers and support cap can be secured. The hole-side does not need to be checked as the free rotation condition is very easy to maintain. However, for each test the support tower on the slot-side must be disconnected from the slip table and forced along the lateral direction until it is free to translate along the slot. The support tower can then be reconnected to the slip table.

Once the specimen is in place and fully clamped, the masses can be moved to touch the specimen and the pneumatic cylinders can be pressurized. It is important to adjust the pressure in both cylinders equally as not to bend or deform the specimen in any manner. This can be done by simply turning both valves slowly at the same time. The pressure is measured in each cylinder by the pressure transducers and their output is displayed on an oscilloscope. The regulator is tweaked until the desired pressure (which can vary depending on the test) is reached. The eddy current sensor can then be positioned. If the experiment is a fatigue test, then the sensor mount is pressed set against the sensor plate with a shim of thickness 0.584 mm and the mount can then be tightened. Because the condition for failure is met when the beam deforms to a certain distance from the sensor it is very important to keep the initial distance between the sensor and the specimen as consistent as possible for all fatigue tests. Otherwise, if the eddy current sensor is to measure the displacement of one of the masses for a system identification test, the sensor can be located close to the mass plate; the output from the sensor should be around 4-5 V.

The setup is now complete and the shaker can be connected to the output signal. It is very important to never connect the shaker to a live output signal. Also, the gain of the signal must always be slowly ramped up to avoid sudden input jumps which can damage the shaker. The PC LabView program can be started and data collection will begin. An Excel report will automatically be generated and the operator can fill in pertinent information.

2.4 Modal Analysis

Modal Analysis is used during the system identification process. The test setup is quite different from the previously defined system. The modal analysis is used during the system identification procedure to detect nonlinearity in the system. An ACE data acquisition card and Signal Calc modal analysis software from Data Physics is used. The frequency response function (FRF) is calculated from data averaged over 16 windows of burst-random excitation. This excitation was chosen to mitigate spectral leakage. Eighty percent of the window size is dedicated to random excitation, while the remaining twenty percent is zero-level excitation. In the experiments, the input signal was from an accelerometer mounted to a rigid support, while the output signal was from an accelerometer mounted to the front mass. Both signals are high pass filtered at 5Hz in order to remove low frequency uncertainties related to accelerometers.

2.5 Algorithm: PSW and SOD

Recorded scalar fast-time accelerometer data, $\{y(n)\}_{n=1}^{M}$, is collected over consecutive data records of length $t_D = Mt_s$, where t_s is the sampling frequency (1 kHz in this case) of the DAQ system and M is the number of points in each data record. The size of each data record is large enough to adequately describe the fast-time dynamics of the system. The fast-time phase space of the scalar time series $\{y(n)\}$ is then reconstructed using delay coordinate embedding where $\boldsymbol{y}_n = [y(n), y(n+\tau), ..., y(n+(d-1)\tau)]^{\mathrm{T}} \in \mathbb{R}^d$, where τ is the time delay based on average mutual information, d is the embedding dimension based on the method of

false nearest neighbors and **T** is used to denote transpose. The embedding parameters are determined using techniques discussed in (Kantz, Holger, & Schreiber, 2004).

A metric which is in one-to-one smooth relationship with damage variables in the reconstructed fast-time phase space is needed. That metric is first introduced in (Chelidze, Cusumano, & Chatterjee, 2002) and is further extended in a multidimensional form in (Chelidze & Cusumano, 2004). The metric provides a measure of deformation of the fast-time phase space trajectories due to slow time parameter drift. A detailed discussion is provided in (Chelidze & Cusumano, 2006), advocating the advantages of the short-time statistic over conventional long-time statistics. The metric is called the *phase space warping function* (PSWF) and is defined as

$$e_R(\phi; \boldsymbol{y}_n) \triangleq \boldsymbol{y}_{n+1} - \boldsymbol{P}(\boldsymbol{y}_n; \phi_R), \tag{2.1}$$

where $\boldsymbol{y}_n$ is a point in the reconstructed phase space for the current damage state $\boldsymbol{\phi}$; $\boldsymbol{y}_{n+1}$ is its image one time step later; and $\boldsymbol{P}(\boldsymbol{y}_n; \phi_R) \triangleq y_{n+1}^R$ is the image of $\boldsymbol{y}_n$ for a reference or healthy damage state ϕ_R.

In (Chelidze & Cusumano, 2004), for developing a multi dimensional tracking vector, it was proposed to partition the phase space into small disjoint hyper cuboids $(B_i, i = 1, \dots, N_d)$ and evaluate the expected value of the PSWF in each region,

$$e_i(\phi) = \frac{1}{N_i} \sum_{y \in B_i} \hat{e}\,(\phi; \boldsymbol{y}), \tag{2.2}$$

where N_i is the number of points in B_i and ê is an estimate of the PSWF, using some data-based model for $\boldsymbol{P}(\boldsymbol{y}, \phi_R)$. All these averaged PSWF's are assembled into an $m = dN_d$-dimensional feature vector for each observation $\{j\}_{j=1}^{q}$,

$$\boldsymbol{e}^j = \left[e_1(\phi); e_2(\phi); \ldots; e_{N_d}(\phi)\right], \tag{2.3}$$

where semicolons indicate column-wise concatenation.

It was demonstrated in (Chelidze & Cusumano, 2004) that these feature vectors can be projected onto actual damage states if the total change in the damage state is small. The feature vectors were stacked in a time sequence as row vectors into a *tracking matrix* $\boldsymbol{Y} \in \mathbb{R}^{\boldsymbol{q} \times \boldsymbol{m}}$. It was then observed that SOD of this tracking matrix provided the reconstructed damage phase space that was in direct relationship with the actual phase space.

SOD is performed using general singular value decomposition of the matrix $\boldsymbol{Y}$ and its time derivative $\boldsymbol{DY}$, where $\boldsymbol{D}$ is a discrete differential operator:

$$\boldsymbol{Y} = \boldsymbol{UCX}^{\mathrm{T}} \text{ and } \boldsymbol{DY} = \boldsymbol{VSX}^{\mathrm{T}}, \tag{2.4}$$

where $\boldsymbol{U}$ and $\boldsymbol{V}$ are unitary matrices; $\boldsymbol{C}$ and $\boldsymbol{S}$ are diagonal matrices; and $\boldsymbol{X}$ is a square matrix. The *smooth orthogonal coordinates* (SOCs) are given by the columns of $\boldsymbol{\Phi} = \boldsymbol{UC}$, *smooth orthogonal modes* (SOMs) are provided by the columns of $\boldsymbol{\Psi} = \boldsymbol{X}^{-\mathrm{T}}$ and *smooth orthogonal values* (SOVs) are $\sigma = \mathrm{diag}(\boldsymbol{C}^T\boldsymbol{C})/\mathrm{diag}(\boldsymbol{S}^{\mathrm{T}}\boldsymbol{S})$. The dominant SOVs hold information about the dimensionality of damage phase space and the corresponding SOCs reconstruct that phase space. In (Chelidze 2005) and (Chelidze

2006) this algorithm was successfully applied to the tracking and prediction of fatigue damage evolution.

2.6 Surrogate Data

A surrogate time series is generated using an algorithm designed to preserve certain statistics and characteristics of the original time series. The algorithm used in this study is introduced in (Schreiber & Schmitz, 1996). The purpose of using surrogate data is typically for the detection of nonlinearity (Kantz, Holger, & Schreiber, 2004). The algorithm has been adopted for this research in order to compare damage due to chaotic and random loading. It is necessary to study two signals with the same probability distribution (accordingly mean and variance and all other related statistics will be preserved) and *power spectrum density* (PSD). The time history, however, will be randomized.

It is very easy to randomize the time history and almost as easy to preserve the PSD. However, an iterative process is required to meet the desired conditions. Throughout this process the subscript k is used to denote a list of indices, n, decided by the sorting of the magnitudes of the series in question. The first step in the algorithm is to store a copy of the original data, $\{x_n\}_{n=1}^{N}$, sorted by magnitude, $\{c_k\}$ as well as the amplitudes of the Fourier transform of the data, $\{|S_n|^2\}_{n=1}^{N}$. To begin, there is a random shuffle of the data to give $\{r_n^0\}_{n=1}^{N}$, where the superscript indicates the iteration. The iteration is as follows:

1) The Fourier transform of $\{r_n^i\}_{n=1}^N$ is taken, the amplitudes are replaced with $\{|S_n|^2\}$ and the inverse Fourier transform is performed leaving $\{z_n^i\}$.
2) The first iteration will be repeated after transforming $\{z_n^i\} \rightarrow \{r_n^{i+1}\}$ by replacing the sorted magnitudes $\{z_k^i\}$ with $\{c_k\}$ to get $\{r_k^i\}$ and re-ordering $\{r_k^i\} \rightarrow \{r_n^{i+1}\}$.

The surrogate will have exactly the same probability distribution, with a very close PSD. As the number of iterations increases the error between the PSDs of the original and surrogate series will converge to some minimal error.

2.7 Cycle Counting

A very simple rainflow counting algorithm is implemented. The main objective of rainflow counting is to break a variable load history signal into an equivalent sequence of constant amplitude cycles. Once cycle counting is performed the linear Palmgren-Miner damage law can be applied for fatigue life predictions. The algorithm outlined here is described in (Downing & Socie, 1982).

The algorithm is intended for analyzing data after collection has been completed, and not real time computations. Two rules, which define the range of each peak and valley, must be kept in mind throughout the algorithm:

$$X = \text{range under consideration}$$

$$Y = \text{previous range adjacent to } X$$

Each peak or valley is put in a vector $\boldsymbol{E}(n)$ as it is encountered.

The history must first be rearranged to begin and end with the maximum peak (or minimum valley). Four simple states are then used to count the cycles; they are as follows:

1) Read the next peak or valley; stop if out of data.
2) Form ranges X and Y; if the vector contains less than three points go to 1.
3) Compare ranges X and Y
    a. If $X < Y$, go to 1.
    b. If $X \geq Y$, go to 4
4) Count range Y; discard the peak and valley of Y; go to step 2.

The algorithm then gives the equivalent cycles once all peaks and valleys have been discarded and no data remains.

CHAPTER 3

SYSTEM IDENTIFICATION

In this chapter a *system identification* (SID) approach is implemented in order to characterize and better understand the new system. The goal is to develop a reliable model of the healthy structure. A three step process (which includes detection of nonlinearity, model selection, and parameter estimation) is adopted. Also additional discussions about nonlinearity will be provided.

3.1 Detection of Nonlinearity

The ability to detect nonlinearity has potential applications in structural health monitoring. Related approaches are reviewed in [Farrar 2007]. The *frequency response function* (FRF) overlay approach was used in this case. The concept of this approach is that the FRF of a linear system is independent of excitation amplitude. This, however, is not true for a nonlinear system. Therefore, nonlinearity can be detected by changes in the FRF associated with changes in excitation amplitude.

Standard modal analysis is conducted as described in section 2.4. Three tests were conducted at amplitude levels small, medium and large. The corresponding FRF's are shown in Figure 7. With the increase of excitation amplitude the peak of the FRF clearly shifts towards the lower frequency range. This is indicative of a softening spring behavior.

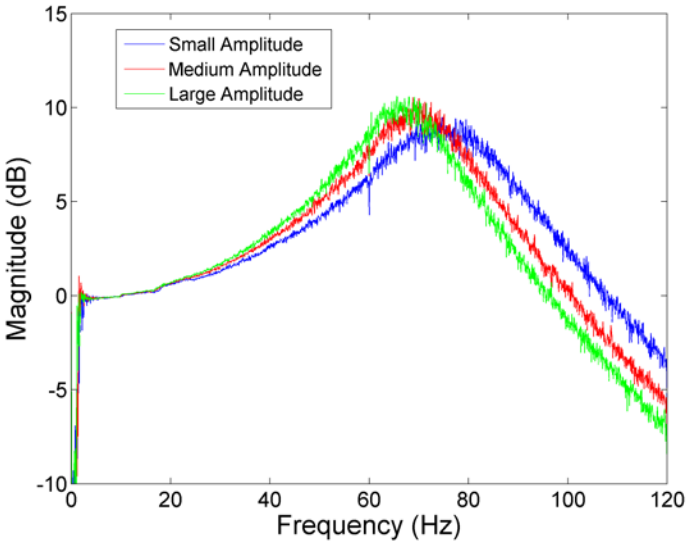

Figure 8. Frequency response function with varying excitation amplitudes.

3.2 Nonlinear Model Selection

The major challenge of nonlinear system identification is model selection (Hong, Mitchell, Chen, Harris, Li, & Irwin, 2008). Because the system is not very complicated, a two step procedure is adopted to determine a system model. The first step is to build a simple physical model with some unknown functions. The method of the Restoring Force Surface (RFS) will then be used as the second step to determine the unknown functions.

The assumptions that the slip table and fixtures are rigid, and the deformation of the specimen is relatively small ($< 2 \times 10^{-4}$ m from its equilibrium position), allows the testing rig to be represented by a single degree of freedom mass-spring-damper system shown in Figure 8.

The specimen is modeled as a linear spring (with stiffness k_s). The pneumatic cylinders are represented by a combination of nonlinear springs (k_1 and k_2) and

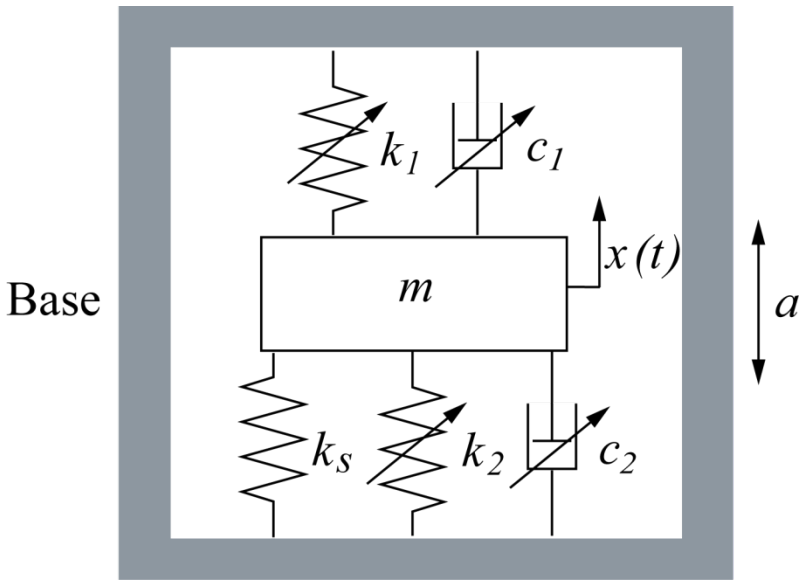

Figure 9. Simplified mass-spring-damper model of the fatigue testing apparatus.

nonlinear dampers (c_1 and c_2). The system can be described by the differential equation in the form of:

$$m\ddot{x} + c_1(x,\dot{x}) + c_2(x,\dot{x}) + k_1(x,\dot{x}) + k_2(x,\dot{x}) + k_s x = ma \tag{3.1}$$

where, m is the addition of the two masses; a is the base acceleration; x is the relative displacement measured by the eddy current sensor, and dots represent time differentiation. Further simplification can be made resulting in:

$$m\ddot{x} + C(x,\dot{x}) + K(x,\dot{x}) + k_s x = ma \tag{3.2}$$

where $C(x,\dot{x}) = c_1(x,\dot{x}) + c_2(x,\dot{x})$ and $K(x,\dot{x}) = k_1(x,\dot{x}) + k_2(x,\dot{x})$.

Restoring force is defined as a variable force that gives rise to equilibrium in a physical system and can be written as:

$$f(x,\dot{x}) = F - m\ddot{x} \tag{3.3}$$

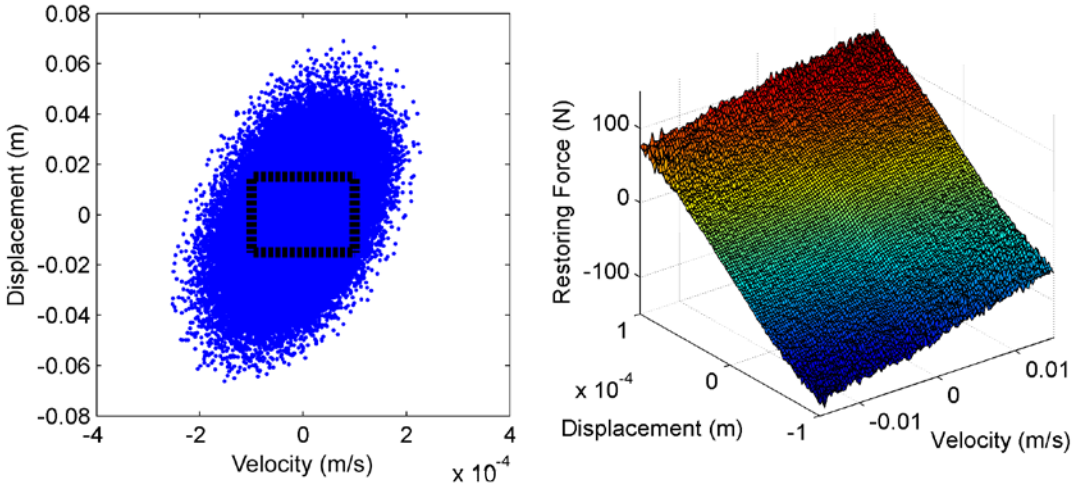

Figure 10. The distribution of data points within the phase plane (left). The data used to generate the Restoring Force Surface (right) is outlined by the dark dashed box.

for a SDOF system, where F is the external force and m is the mass. In our case, the restoring force equals:

$$f(x,\dot{x}) = -ma - m\ddot{x} = C(x,\dot{x}) + K(x,\dot{x}) + k_s x \tag{3.4}$$

The related *restoring force surface* (RFS) approach is one of the most well established nonlinear system identification methods available. Although we do not plan to apply the RFS method directly, the RFS can provide valuable information for model selection. Among all the parameters, mass is measured directly, a is measured by an accelerometer, x can be measured by the eddy current sensor, and $\dot{x}$ and $\ddot{x}$ can be estimated using the finite difference method. Therefore, the RFS can be directly generated based on collected data sets.

The restoring forces are calculated using 6×10^5 data points, while the testing rig is driven by a random signal with limited frequency band (0 to 60Hz). The amplitude of the excitation was chosen to ensure the availability of parameter identification data within the range of proposed experimental excitation amplitudes. The pressure in the

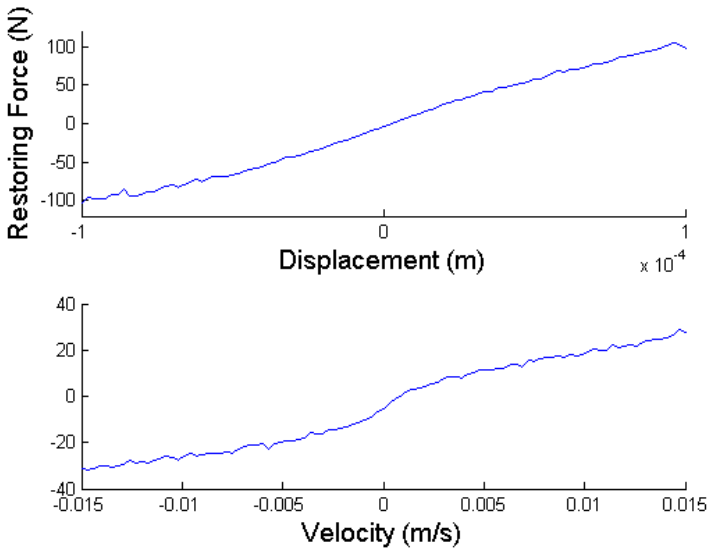

Figure 11. Slice view of the RFS at $\dot{\boldsymbol{x}} = \mathbf{0}$ (top) and $\boldsymbol{x} = \mathbf{0}$ (bottom)

two pneumatic cylinders is set to 103 kPa. The data is recorded at a DAQ frequency of 1 kHz and the distribution of sample points on the phase plane are shown in Figure 9.

Isolated points related with discrete measurements are interpolated into a continuous surface using Sibson's natural neighbor method (Sibson, 1985), and the measured RFS is shown in Figure 9.

Two slice views of the RFS are shown in Figure 10 with $x = 0$ and $\dot{x} = 0$ respectively. It is a reasonable assumption that $C(x, \dot{x})$ is a function of $\dot{x}$ only and $K(x, \dot{x})$ is a function of x only; $f = C(\dot{x})$ when $x = 0$ and $f = K(x) + k_s x$ based on this assumption. From Figure 10, we can conclude that $C(\dot{x})$ and the $K(x)$ can be described partially by cubic polynomials. However, it is also suspect that Coulomb damping is present in the system. A good experimental fit of the restoring force with Coulomb damping (Olsson, Astrom, Canudas de Wit, Gafvert, & Lischinsky, 1998) can be described as

$$F = C|\dot{x}|^{\delta_v}\text{sgn}(\dot{x}) \tag{3.5}$$

where F is the restoring force and δ_v is a scaling parameter dependent on geometry. Therefore, equation 3.2 can be rewritten in the form:

$$m\ddot{x} + C_{f1}\dot{x} + C_{f2}\dot{x}^3 + C_{f3}|\dot{x}|^{\alpha}\text{sgn}(\dot{x}) + K_{f1}x + K_{f2}x^3 + K_{f3}|x|^{\beta}\text{sgn}(x) = ma \tag{3.6}$$

where $C(\dot{x}) = C_{f1}\dot{x} + C_{f2}\dot{x}^3 + C_{f3}|\dot{x}|^{\alpha}\text{sgn}(\dot{x})$ and, $K(x) = K_{f1}x + K_{f2}x^3 + K_{f3}|x|^{\beta}\text{sgn}(x)$.

3.3 Parameter Estimation

With a nonlinear model, the system parameter estimation problem can be solved. The method of *direct parameter estimation* (DPE) (Mohammad, Worden, & Tomlinson, 1992) will be used. To perform DPE, Eq. 3.6 is rewritten for n discrete measurements in the form of Eq. 3.7. However, because of the exponents, α and β, the error must be reduced iteratively. DPE is performed while varying α and β over a predetermined range in order to minimize the mean square error.

$$\begin{bmatrix} \dot{x}_1 & \dot{x}_1^3 & |\dot{x}_1|^{\alpha}\text{sgn}(\dot{x}_1) & x_1 & x_1^3 & |x_1|^{\beta}\text{sgn}(x_1) \\ \dot{x}_2 & \dot{x}_n^3 & |\dot{x}_2|^{\alpha}\text{sgn}(\dot{x}_2) & x_2 & x_2^3 & |x_2|^{\beta}\text{sgn}(x_2) \\ \vdots & \vdots & \vdots & \vdots & \vdots & \vdots \\ \dot{x}_n & \dot{x}_n^3 & |\dot{x}_n|^{\alpha}\text{sgn}(\dot{x}_n) & x_n & x_n^3 & |x_n|^{\beta}\text{sgn}(x_n) \end{bmatrix} \begin{bmatrix} C_{f1} \\ C_{f2} \\ C_{f3} \\ C_{f4} \\ C_{f5} \\ C_{f6} \end{bmatrix} = \begin{bmatrix} \ddot{x}_1 & a_1 \\ \ddot{x}_2 & a_2 \\ \vdots & \vdots \\ \ddot{x}_n & a_n \end{bmatrix} \begin{bmatrix} m \\ -m \end{bmatrix} \tag{3.7}$$

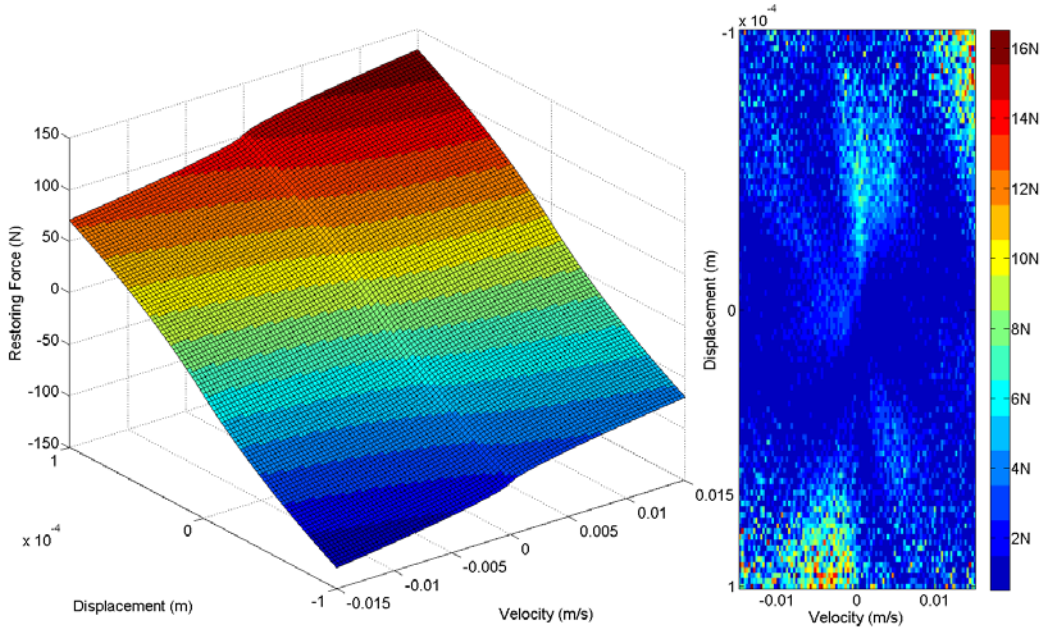

Figure 12. The RFS based on the nonlinear system model (left) and the error between the modeled surface and the calculated RFS (right).

When $n > 6$ this is an over defined problem which can be solved by using a standard least squares approach. The parameters are determined using the data shown in Figure 9. An RFS can then be generated based on the identified nonlinear model. The resulting surface and the error, between the modeled surface and the RFS, are shown in Figure 11. The results are reasonable and the error is quite low ($< 16N$ or 10 %).

Although the two RFS's (based on the measured data and based on the model) fit each other quite well, relatively large errors are observed in the areas when the absolute value of x and $\dot{x}$ are large and $(x/\dot{x}) > 0$. The large errors are due to three main reasons:

1) The number of sampling points in these areas is small, which leads to inaccurate estimation of the RFS from experimental data.

2) These areas represent rare dynamical states of the rig; large displacement, velocity, acceleration, and jerk, which make the numerical calculation of velocity and acceleration inaccurate.
3) With a large jerk, $\dddot{x}$, a time delay between different measurement channels on the DAQ system is not negligible and causes additional errors in the measurement of acceleration.

3.4 Discussion

3.4.1 Dynamic Range

The system has the capacity to generate 1.6 g's of acceleration at 30 Hz. The maximum load capacity is determined by the mass of the inertial blocks and the maximum acceleration of the slip table. Theoretically, there is no limitation to the frequency range of the load if the slip table and all fixtures can be treated as rigid bodies. However, the highest frequency of applied load in real tests is limited to 30 Hz because the natural frequency of the slip table is about 150 Hz. Further improvement of the structural stiffness is not pursued, because higher stiffness means additional mass for the slip table; and as a result, the maximum load capacity will decrease due to the limitation of the shaker output power.

3.4.2 Influence of Air Pressure

The same system identification procedure is repeated several times under different pressures (the pressure in the two cylinders is kept identical). The estimated parameters are listed in Table 1. The relationship between the pressure and the system

parameters can be described as follows: the stiffness and the damping of the testing system increase when pressure is increased.

Table 1. Results of Direct Parameter Estimation with varying cylinder air pressure.

Press (kPa)	$C_{f1}\left(\frac{Ns}{m}\right)$	$C_{f2}\left[\left(\frac{Ns}{m}\right)^3\right]$	$C_{f3}\left[\left(\frac{Ns}{m}\right)^\alpha\right]$	$K_{f1}\left(\frac{N}{m}\right)$	$K_{f2}\left(\frac{N}{m^3}\right)$	$K_{f3}\left(\frac{N}{m^\beta}\right)$	α	β
138	400.58	-6.48×10^4	342.04	1.41×10^6	8.72×10^{12}	-8.96×10^8	0.63	1.81
172	-4.18×10^3	1.87×10^4	3.19×10^3	2.31×10^6	4.56×10^{13}	-7.80×10^9	0.82	1.93
207	-2.36×10^3	-6.96×10^4	2.06×10^3	2.25×10^6	3.99×10^{13}	-1.56×10^{10}	0.79	2.02

3.4.3 Linear Region

The system has been characterized to have nonlinear stiffness and damping. Coulomb damping is strong at a small velocity and displacement level. However, when the system is observed over a relatively narrow range of displacement and velocity the system appears to be approximately linear. The definition of a linear region is also interesting theoretically since 1) there is an advantage in system analysis if a linear assumption holds, and 2) a change of the linear region boundary itself can serve as an indicator for abnormality.

Here non-linearity is defined by how accurately a linear model can fit the measured RFS. For a region R_G in the phase space defined by $|x| < x_1$ and $\dot{x} < x_2$, a linear model is estimated based on Eq. 3.7 by assuming that only C_{f1} and K_{f1} are nonzero. The nonlinearity (N) is quantified by

$$N = \frac{\max\ |f(x,\dot{x})_l - f(x,\dot{x})_m|}{\max\ |f(x,\dot{x})_m|} \tag{3.8}$$

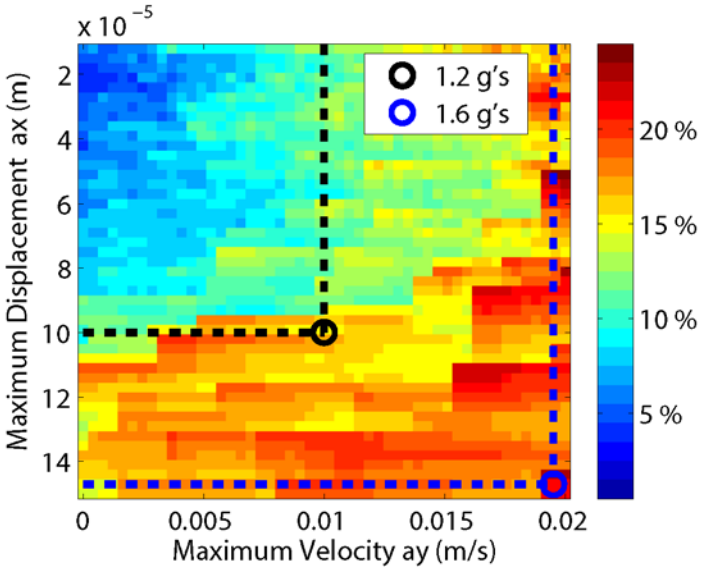

Figure 13. Relationship between nonlinearity and vibration amplitude.

where $[x, \dot{x}] \in R_G$, $f(x, \dot{x})_l$ is the restoring force calculated based on the linear model, and $f(x, \dot{x})_m$ is the measured restoring force.

Based on the above definition, the nonlinearity of different regions on the response phase space is shown in Figure 12. For each pixel on the image, its coordinates (ax and ay) define the region on the response phase space $|x| < ax$ and $|\dot{x}| < ay$ and its color illustrates the severity of the nonlinearity. A color bar is provided with the map to allow for convenient interpretation of the data. Nonlinearities under a 20 Hz sinusoidal excitation at amplitudes of 1.2 g and 1.6 g are outlined in black and blue circles respectively. Since a 1.2g excitation is representative of a typical experiment (1.6g is a higher limit) and its corresponding nonlinearity is relatively low ($< 15\%$), we can conclude that the testing rig works in a linear region under a typical load condition.

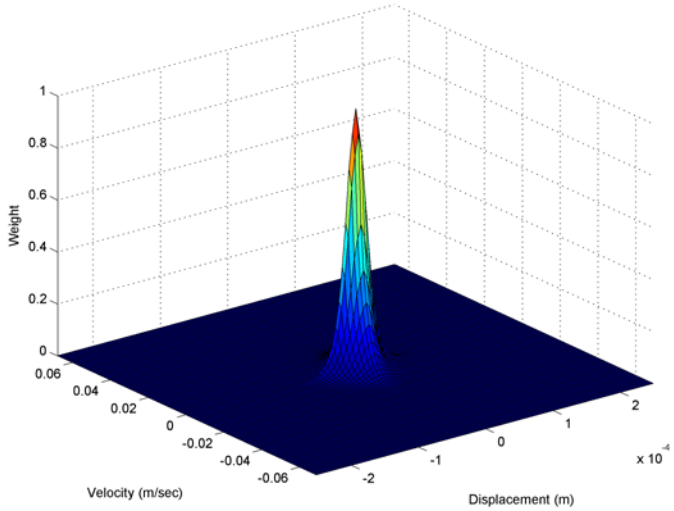

Figure 14. Weighting function based on the distribution of data used to perform weighted least squares for DPE, accentuating areas with a large amount of data.

3.4.4 Verification

The restoring force surface method can be verified by comparing DPE with standard linear modal analysis approaches. As outlined previously, modal analysis can be used because it is reasonable to treat the system as a linear system if the response amplitude is low. Verification of the restoring force method will be completed if the results from DPE and modal analysis fit each other well.

In order to directly compare the results of the two methods, short experiments were run using Signal Calc modal analysis software from Data Physics. In these experiments, the response amplitude is controlled carefully, so the linear assumption can be held. The FRF data, collected using the same parameters outlined in Section 3.1, can be fit to the known single degree of freedom FRF in the form:

$$|G(i\omega)| = \frac{C_s}{\sqrt{(1-r^2)^2 + (2\zeta r)^2}} \tag{3.9}$$

where $G(i\omega)$ is the frequency response, C_s is a scaling factor, ζ is the damping ratio, and r is ω/ω_n. The parameters, C_s, ζ, and ω_n are approximated using an iterative method which minimizes the least squares error. In order to emphasize the significance of the data at areas of small velocity and displacement, a weighted least squares approach was used for DPE. The weighting function is a 3-dimensional surface which is representative of the distribution of data across the phase space (3-dimensional histogram). The function is normalized giving each data point a weight between zero and one, depending on where in the phase space it exists. The weighting factor is

$$W = (w_1 w_2) \tag{3.10}$$

where W is the weight function shown in Figure 13, $w_1$is the distribution function of x and w_2 is the distribution function of $\dot{x}$. The natural frequency is then calculated using the measured mass and the linear coefficient of stiffness, K_{f1}. The results can be seen in Table 2.

Table 2. Verification of RFS method by comparison of natural frequency estimations.

	Modal Analysis	Restoring Force
Pressure (kPa)	ω_n (Hz)	ω_n (Hz)
138	86.27	91.45
172	88.45	92.11
207	106.24	104.04

Chapter 4

FATIGUE EXPERIMENTS

The main purpose of the novel fatigue apparatus is to study the relationship between fatigue crack evolution and system dynamics. The design work and system identification prove that this system is capable of meeting the goals of the research and will be useful for further endeavors, including the study of predictive models of fatigue failure based on fast-time system dynamics data. This ambitious goal cannot be met in this work. The scope of this thesis is not to compile such a model, but rather to serve as a foundation of further modeling efforts and demonstrate the effectiveness of the apparatus.

As mentioned in the introduction one of the research goals is to observe the interplay between structural dynamics and fatigue damage for statistically matched chaotic and random excitations. It was hypothesized that there will be an incommensurate relationship between the *time to failure* (TTF) of the specimens under the two signal types. In order to explore this hypothesis, fatigue experiments were conducted at two amplitude levels (high and low with maximum base acceleration of 1.7 and 1.5 g's respectively) and the results will be discussed in separate sections. It was also declared that the rainflow counting method would be utilized in combination with the Palmgren-Miner rule to investigate the appropriateness of linear damage models. The hypothesis is that this type of damage law will not reflect the results of the fatigue life experiments.

4.1 Signal Generation

A chaotic signal was generated from the equations describing the Duffing oscillator, which can be written as a periodically forced oscillator with nonlinear stiffness:

$$\ddot{x} = -\delta\dot{x} + \beta x - \alpha x^3 + \gamma\cos(\omega t) \tag{4.1}$$

where δ is the damping constant, β is the negative stiffness constant, α is the nonlinear stiffness constant, and γ is the forcing amplitude. The parameters are chosen such that the system will be in a chaotic state. This can be shown by plotting a bifurcation diagram of the system. In this case from the bifurcation diagram the system is chaotic for the parameters $\alpha = 1, \beta = 0.6, \delta = .25, \gamma = .2$, and $\omega = 1$.

Once the time series is generated in Matlab a nearest neighbor search is done to find a similar state further in time. This is necessary in order to match the start and end point of the time series as closely as possible. The function generator used to output the signal to the shaker can only handle a maximum of 2^{16} data points so the signal is looped throughout the testing. Once the ends are matched up with a sufficiently large amount of data between them, the time series is exported as a ASCII text file and imported into Tektronix' ArbExpress waveform generation software. There, the signal is exported to a USB flash drive which will be used to load the signal onto the function generator.

Because the signal is repeated periodically, the frequency of the function generator must be set to keep the frequency of the input excitation where it is desired

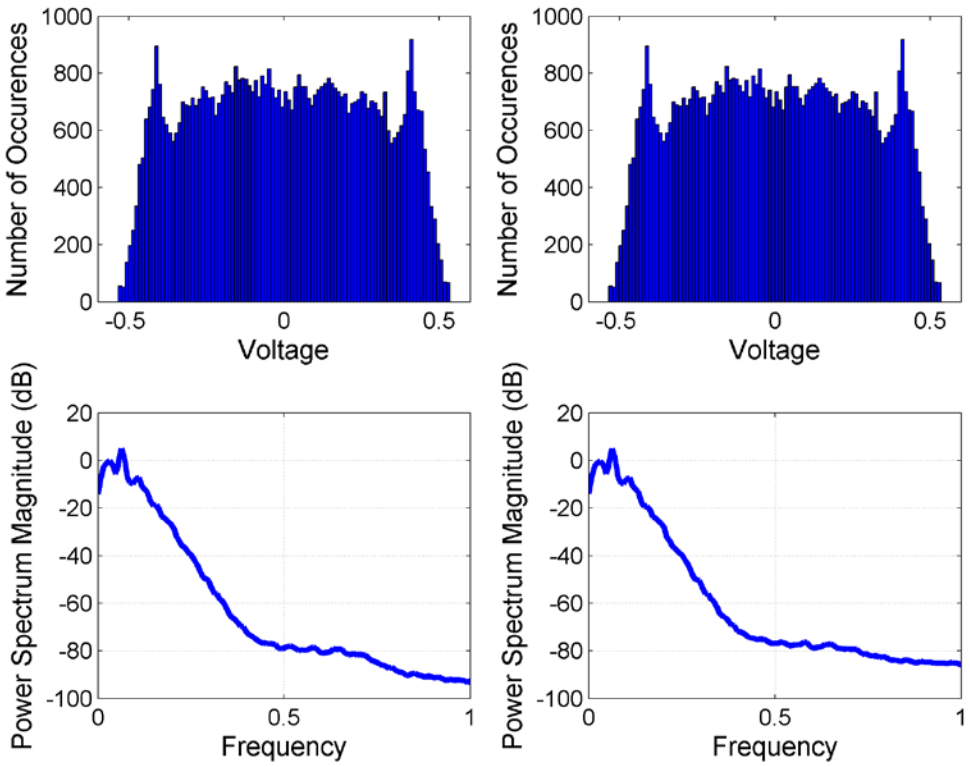

Figure 15. Comparison of the original chaotic and surrogate data signals (left and right columns respectively). Histogram of the time series data (top row) periodogram of the time series (bottom row).

(approximately 20-30 Hz). This is done by collecting the output of the function generator, set at some frequency, and processing the data to get the power spectrum. The function generator frequency is adjusted until the main frequency components of the power spectrum fall within the desired range. For this particular signal it was found that the frequency must be set to 20 mHz. The surrogate data set can then be generated from the chaotic time series by using the algorithm included in section 2.6.

4.2 High Amplitude Fatigue Tests

The excitation amplitude was decided to keep the tests concise for quick turnaround time. It is also beneficial to have relatively short data sets to save on digital storage and computation time during data analysis. It should be noted that all

Table 3. High amplitude test results. Mean, variance, and power are calculated from base acceleration data over 12 data records. Power is a simple sum of the squares.

Test Number	Excitation Signal	Time To Failure (hrs:min)	Mean (V)	Variance (V^2)	Power (V^2)
1-A	Random	0:53	−0.0036	0.0754	9.05×10^4
1-B	Chaotic	1:44	−0.0030	0.0728	8.74×10^4
2-A	Random	1:07	−0.0036	0.0724	8.70×10^4
2-B	Chaotic	1:50	−0.0038	0.0725	8.70×10^4
3-A	Random	0:44	−0.0035	0.0758	9.09×10^4
3-B	Chaotic	1:46	−0.0034	0.0735	8.82×10^4
4-A	Random	0:52	−0.0036	0.0763	9.15×10^4
4-B	Chaotic	1:42	−0.0037	0.0729	8.75×10^4
5-A	Random	0:45	−0.0040	0.0735	8.82×10^4
5-B	Chaotic	1:13	−0.0039	0.0725	8.71×10^4

test names are indicative of the order run and no further inference should be made. Also, the two signals used for driving the system are henceforth called Chaotic and Random, and it should be implicit that these signals are varied only in amplitude. The experimental design is very straightforward. A minimum of five successful tests will be accepted for each excitation type. This will result in a total of ten sets of data for analysis at the high amplitude level.

The first and most obvious piece of data that gives an indication of the fatigue process is the TTF. A clear trend emerges in the TTF data shown in Table 3. It is obvious that the Random excitation is much more damaging to the specimen. These test results show that the system under Chaotic excitation outlasts the system under Random excitation by nearly a factor of two in all accounts. This data appears to be

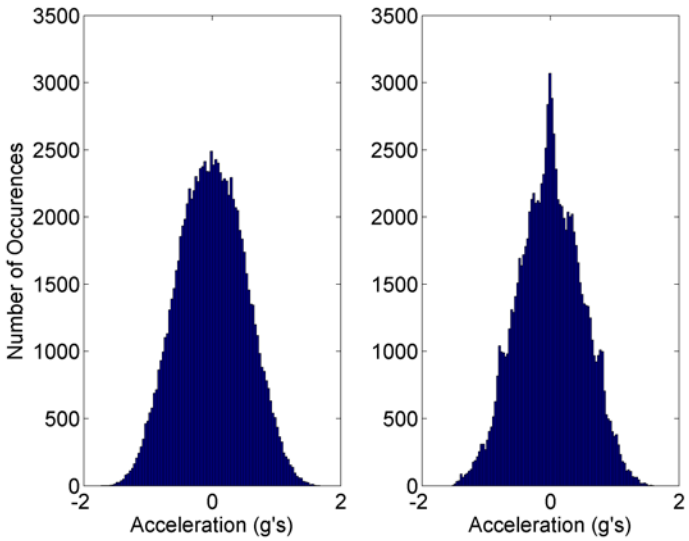

Figure 16. Histogram of the base acceleration data of the Random and Chaotic signals (left and right respectively.)

very interesting and supportive of the hypothesis that there is a strong relationship between fatigue accumulation and time history.

The statistics are included in Table 3 to show that the statistical qualities of both signals match well. Any drift in these statistics, from test to test, is due to the lack of a sophisticated shaker output controller, however, these tests have proven very repeatable and the variations in the excitation signal seam negligible at this amplitude level. The time histories of one data set of the Random and Chaotic experiments (1-A and 1-B respectively) can be seen in Figure 15. The histograms show base acceleration over one data record. The probability distributions of the output signals match identically; however, the input to the shaker is displacement. The histograms of the acceleration of the base are not then identical under random and chaotic excitation. It would be a very difficult problem to build a surrogate data which would match the transformation of input displacement to acceleration. As long as the main factors such

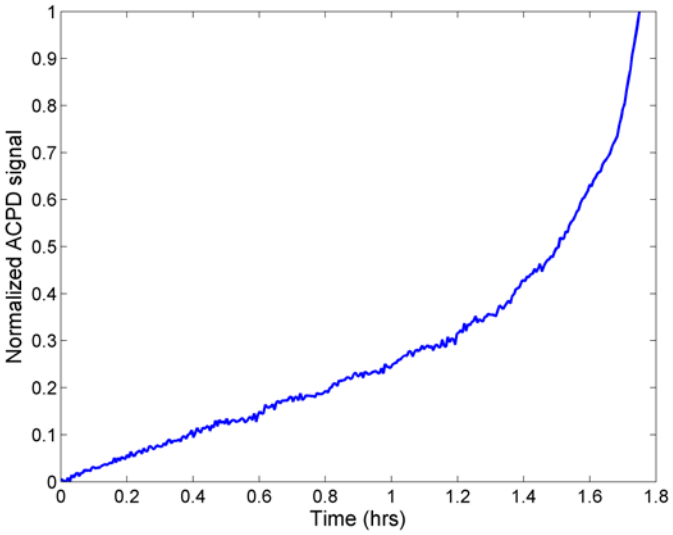

Figure 17. ACPD signal reading normalized for direct comparison to the tracking results. (Results from Chaotic test 1-B)

as mean, and minimum and maximum acceleration are preserved, the differences are acceptable.

4.2.1 Damage Tracking

The real fatigue is tracked using the ACPD measurement equipment. For the high amplitude testing $\{S_n\}_{n=1}^{M}$, where $M = 20{,}000$, is the scalar data record of the ACPD signal. The sampling frequency, t_f, of the DAQ system is 1 kHz; therefore the time length of each data record, $t_s = M/t_f$, is 20 seconds and there are $N = \text{floor}(TTF/ts)$ (TTF is time to failure in seconds) data records in each test. This data is processed by taking the mean of the signal over each data record and concatenating into a vector:

$$ACPD_{sig} = [\{\bar{S}_n\}_1, \{\bar{S}_n\}_2, \ldots, \{\bar{S}_n\}_N] \tag{4.1}$$

The trend can then be plotted as shown in Figure 16.

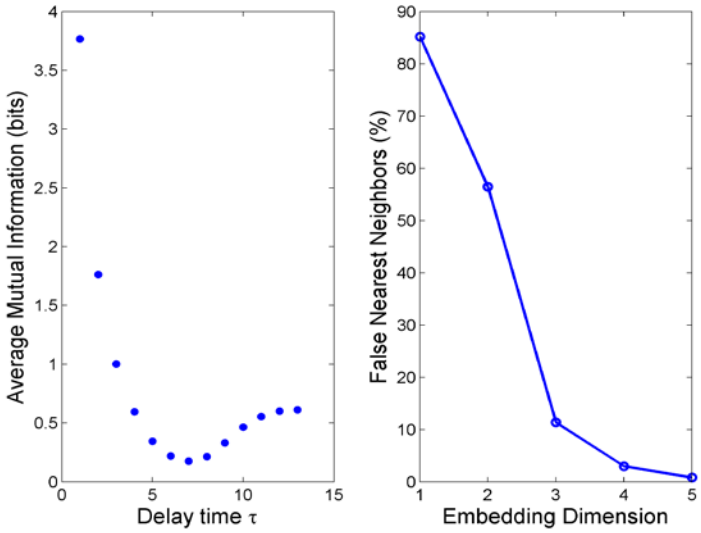

Figure 18. Estimation of embedding parameters using AMI for delay (left) and dimension (right) which are $\boldsymbol{\tau = 7}$ and $\boldsymbol{d = 4}$ (results from test 1-B).

Because the input signal is deterministic, tracking of the damage for Chaotic tests can be done by using the PSW algorithm outlined in section 2.5. As mentioned previously the time series of the mass acceleration $\{a_m\}_{n=1}^{M}$, again $M = 20{,}000$, is used for the fast-time system dynamics data. The time series needs to be embedded using delay reconstruction with the help of the *false nearest neighbors* (FNN) search for embedding dimension, d, (Kennel, Brown, & Abarbanel, 1992) and *average mutual information* (AMI) for the time delay, τ (Fraser & Swinney, 1986). Typically the delay is chosen as the first local minimum of the AMI.

The method of FNN is a straightforward concept. There should be no intersections within the phase space if the system is governed by deterministic differential equations, and points in a small neighborhood should be there due to the dynamics of the system and not insufficient embedding dimension. The FNN method finds the percentage of FNNs in the embedded phase space for a given dimension.

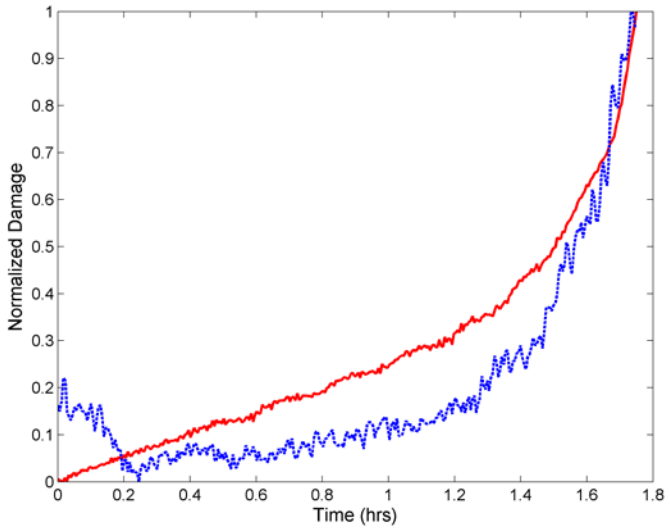

Figure 19. The ACPD signal reading from test 1-B (solid red) and the tracking results of the PSW and SOD (dashed blue). The Damage metrics have been normalized for comparison.

The embedding dimension is decided when the percentage of FNNs are sufficiently small (for example $< 3\%$). The estimation of both parameters using mass acceleration data from test 1-B can be seen in Figure 17.

The PSW algorithm can then be applied. The feature vector is calculated and SOD is applied to track the damage. The results from test 1-B are shown in Figure 18. The damage trend has obviously been captured from the fast-time data, however in many tests the phenomenon evident in the first portion of the tracking metric are observed. It is unclear what causes this effect, but it can be speculated that it is due to some type of "breaking in" of the system. It is possible that the deformation of the beam from the equilibrium position could be the cause of the phenomenon, or perhaps there is an effect of friction between the specimen and adjoining surfaces, or some type of relaxation in the beam from the evolving micro crack distribution.

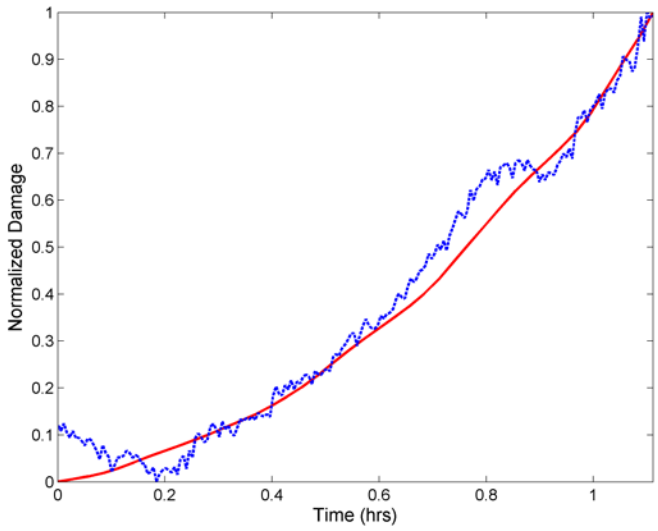

Figure 20. The ACPD signal reading from test 2-A (solid red) and the tracking results of the PSW and SOD (dashed blue). The Damage metrics have been normalized for comparison.

The PSW method will not yield the best results for tracking the fatigue during Random testing. The reason being is that the local linear model tracking metric is not accurate for a randomly excited system. However, because the system can be considered fairly linear under the operating conditions, a linear stochastic *auto regressive* (AR) model can be used to characterize the dynamics. This type of model can be described as:

$$y_n = \sum_{j=1}^{M_{AR}} a_j y_{n-j} + \eta_n \tag{4.2}$$

Where M_{AR} is the order of the model, $\eta_n$is Gaussian white noise, and a_j are the model parameters. These parameters will be calculated for each data record and compose the feature vector used for tracking the parameter drift.

The burg method, implemented in the Matlab function *arburg*, is used to calculate the parameters. The feature vector is assembled as:

$$F = \begin{bmatrix} a_1^1 & a_2^1 & \dots & a_1^N \\ a_2^1 & a_2^2 & \dots & a_2^N \\ \vdots & \vdots & & \vdots \\ a_{M_{AR}}^1 & a_{M_{AR}}^2 & \dots & a_{M_{AR}}^N \end{bmatrix} \tag{4.3}$$

where the feature space, $F \in \mathbb{R}^{M_{AR} \times N}$ and N is the number of data records. SOD can then be applied to track the slow time drift.

The tracked damage metric can be seen in comparison to the ACPD signal in Figure 19. Again, it is clear that the damage has been captured within the fast-time dynamics. Also, it is noted the same phenomenon exists in the beginning of the tracking function. This permeates most test results and it is of interest to determine the causes in the future.

It is also worthy of noting the differences between the fatigue evolution of the Chaotic and Random tests. Due to the time history, there is a very short to nonexistent time span of steady crack growth observed in the Random test data as opposed to the Chaotic results. Fracture is initiated much quicker in the Random testing, hence the shorter fatigue life. The exact causes of this are unknown to the author or available literature, but it can be surmised that the two signals are essentially the same and only unlike one another in time history. Therefore this effect can be described somehow by the information in the time history and reinforces the hypothesis that fatigue life is strongly dependent on time history and not merely probability distribution of stress magnitudes.

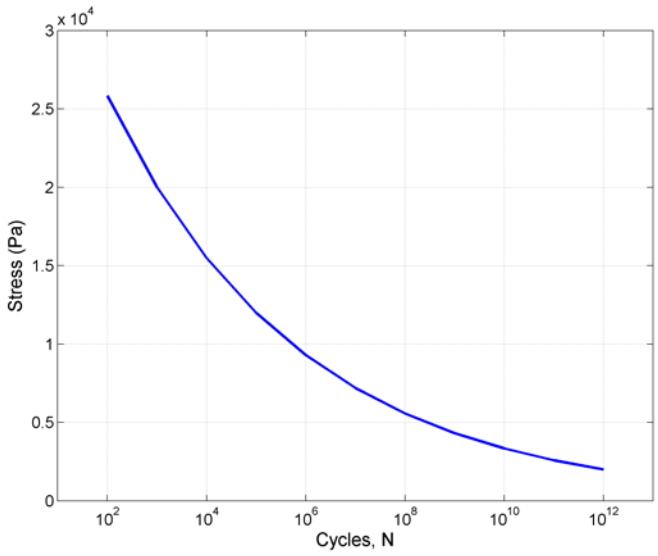

Figure 21. S-N curve used for evaluation of the damage sum, $\boldsymbol{D}$: $\boldsymbol{y = ae^{b\log_{10}(10)}}$ with the parameters $\boldsymbol{a = 4.3 \times 10^4}$ and $\boldsymbol{b = 0.26}$.

4.2.2 Rainflow Counting

Rainflow counting and the Palmgren-Miner rule are used here to quantify the damage based on stress cycles. An S-N curve is necessary to evaluate the Miner rule and find the damage variable. Theoretically, the criteria for failure would occur when the damage variable, D, reaches one. Since D is simply a ratio the exact value depends on the S-N curve used and is inherently nondescript. For the purposes of this research an S-N curve, shown in Figure 20, is assumed based on empirical periodic test results and approximations.

For the short high amplitude tests the cycles of the entire fatigue test are counted. The stress is approximated by simple beam theory. The specimen is regarded as a simply supported beam with an applied load, P, on each side in three point bending. The maximum stress at the notch of the beam is regarded as:

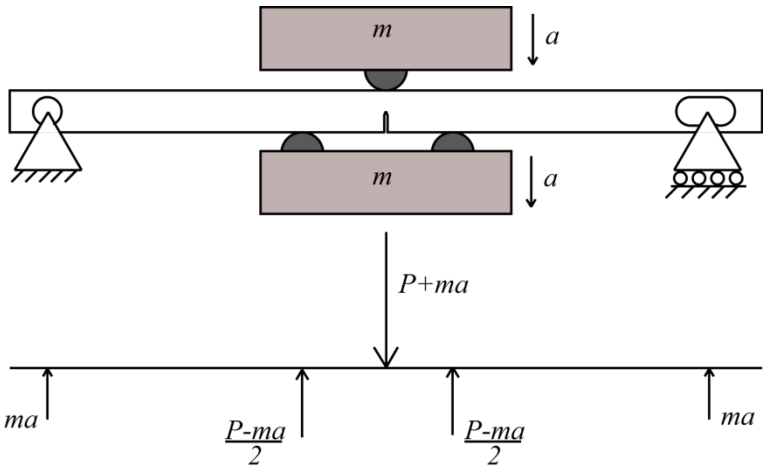

Figure 22. Beam diagram with applied forces. Because of the inertial force the shear and moment distribution changes shape, however we are concerned with the moment (related stresses) at the location of the notch only. *P* is the static force due to the pressure within the cylinders (both cylinders have equal pressure in this testing).

$$\sigma_{max} = \frac{M}{S} \ , \ S = \frac{bh^2}{6} \tag{4.4}$$

Where S is the section modulus, b is the specimen thickness, and h is the width, and

$$M = \frac{P+ma}{4} L_2. \tag{4.5}$$

The load P is

$$P = P_{static} \cong P_c A \tag{4.6}$$

where P_c is the pressure in the cylinder, A is the area of the cylinder's bore. The static load is approximate because of the nonlinearity of the pneumatic cylinder.

The rainflow cycle counting method can then be applied to the time series of the stress data:

$$\sigma_n = \frac{3L_2}{2bh^2}(P + ma) \tag{4.7}$$

The damage variable is then calculated for each test. The results can be seen in Table 4.

Table 4. Damage variables calculated for each test based on rainflow counting and the Palmgren-Miner rule. The Damage variable has been normalized to the average value for the random testing for ease of comparison. Therefore, a damage variable of 1 indicates a failed beam.

Random	TTF (hrs:min)	Damage	Chaotic	TTF (hrs:min)	Damage
1-A	0:53	0.97	**1-B**	1:44	1.54
2-A	1:07	1.07	**2-B**	1:50	2.13
3-A	0:44	1.00	**3-B**	1:46	1.57
4-A	0:52	1.09	**4-B**	1:42	1.49
5-A	0:45	0.87	**5-B**	1:13	1.07
Average	0:52	1.00	**Average**	1:39	1.55

Typically, the Miner rule would be used to predict the failure by characterizing a typical stress history over some time, and approximating the stress history over the expected lifetime of the fatiguing subject. The failure criteria would be met once the damage variable sum was ≥ 1. In this analysis the damage criteria is calculated over the *actual* stress history of the entire time history. Therefore, since the failure criteria is equivalent for all tests it can be expected (if the linear damage law is accurate) that for all tests D would be approximately equal. This is true across tests of the same type, Chaotic or Random, but in comparison between the two the linear damage law does not reflect the effects of the time history. The damage variable should not be

related to time, and the results show a close ratio between TTF and *D*. This implies again that time history is very important in fatigue accumulation.

4.3 Low Amplitude Fatigue Tests

The same signals were run at lower amplitude to investigate the fatigue accumulation over longer test lengths. The results can be seen in the following:

Table 5. Low amplitude test results. Mean, variance, and power are calculated from base acceleration data over 12 data records. Power is a simple sum of the squares.

Test Number	Excitation Signal	Time to Failure (hrs)	Mean (V)	Variance (V^2)	Power (V^2)
6-A	Random	7:25	−0.0043	0.0578	6.94×10^4
6-B	Chaotic	7:20	−0.0049	0.0593	7.12×10^4
7-A	Random	7:28	−0.0050	0.0595	7.15×10^4
7-B	Chaotic	3:49	−0.0049	0.0605	7.26×10^4
8-A	Random	6:51	−0.0040	0.0619	7.42×10^4
8-B	Chaotic	21:06	−0.0041	0.0619	7.43 × 10^4

The TTF results are not as revealing as the previous results. The Random tests are again very consistent; however the Chaotic test results differ drastically. The variations in the signal still exist but are not large and do not appear to have direct relationship to the TTF. For example, the Chaotic test with the longest TTF, 8-B, has the largest power in the signal and variance. If anything in the probability distribution would seem to have a direct impact on TTF it would be these two statistics; however that is not the apparent case.

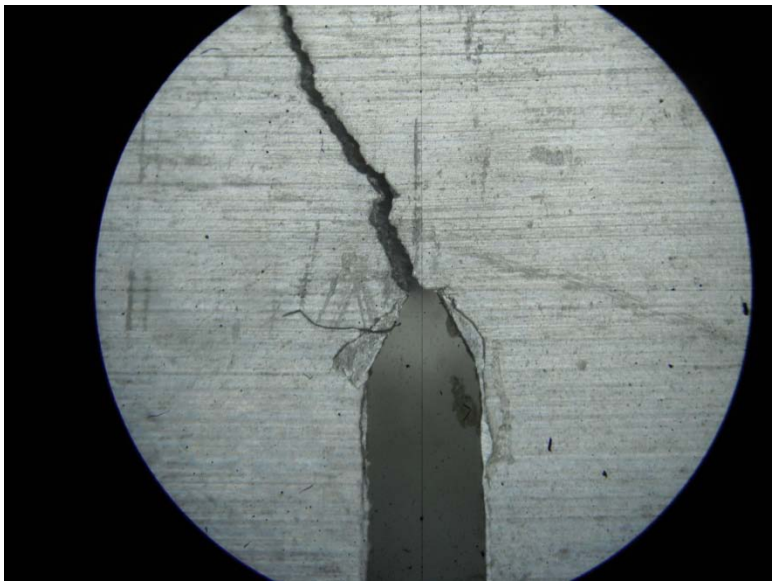

Figure 23. Image of machined notch and fatigue crack at 40X magnification.

The assumption is that the TTF relies heavily on the initial condition. This makes sense and is rather obvious. The controllable condition is the initial cut depth of the notch, and some uncontrollable conditions could be environmental effects, micro crack structure, inherent material stresses, overload induced relaxations etc. The initial crack length was examined under a Stocker and Yale optical micrometer at 40X magnification. The crack lengths of all the fatigue tests recorded in this data were measured to be 7.823 mm ± 0.069 mm, which is relatively consistent and likely not a factor large enough to influence the TTF drastically. This leaves the uncontrollable effects to be the variants in the initial condition. To investigate this further, a much larger sample of data would need to be collected, but it would certainly be an interesting problem to address.

Another notable feature is the fact that in this testing the Random excitation was not always more damaging than the Chaotic. This could possibly be explained by the

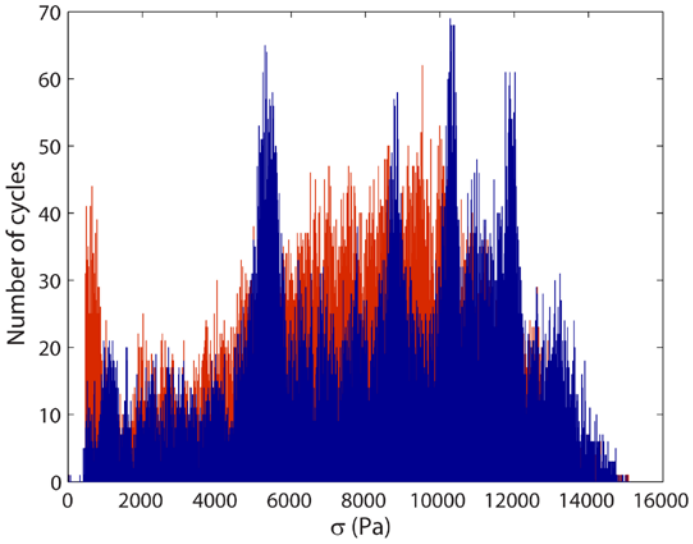

Figure 24. Cycle counting of five data records on tests 8-A and 8-B (red and blue respectively). A larger number of cycle counts in the low stress range are prominent in the Random test, possibly attributing to the longer TTF.

distribution of stress cycles. Using rainflow counting on a data sample comprised of five data records, the stress cycles can be counted and compared. The comparison is between tests 8-B and 8-A. The Chaotic excitation has fewer low stress cycles. This could affect the TTF as the lower stress cycles have much less impact on fatigue accumulation. The reason for the extended TTF of the test 8-B is likely attributed to the initial conditions of the beam, magnified by the lower amplitude.

In general, as the amplitude decreases, the overall shape of the stress cycle distribution would stay the same and simply shift to a lower stress range. Therefore it is expected that the Chaotic excitation would be more damaging at a lower amplitude on average. One test was conducted for a Random and Chaotic excitation at lower amplitude, and this effect was produced; the Chaotic TTF was 12:55 and the Random TTF was 31:06. Further investigation would be necessary to conclude what exactly is

happening, but the stress cycle distribution clearly has a strong relationship with the TTF.

4.4 Discussion of Test Results

It was seen in the high amplitude fatigue tests that the Random excitation produced very consistent time to failures, and was apparently more damaging than the Chaotic excitation. It was also shown, by using an arbitrary S-N curve and a simple rainflow cycle counting algorithm, that the Palmgren-Miner Damage rule was insensitive to the time history. Both of these findings are very interesting and have implications in the real world. From this study it is evident that the Palmgren-Miner rule, which is widely used as an industry standard, is severely lacking in its ability to define damage based solely on a count of stress reversals. It is evident that the order of applied stresses is more damaging in a larger sense than purely frequency or stress amplitudes. It is the recommendation of the author that future tests be conducted with sinusoidal excitation of varying amplitude. This would provide the very simplest scenario to further investigate the effects of stress time history.

Upon further testing, at a lower excitation amplitude, it is seen that the time to failure under Chaotic excitation is much more sensitive to initial conditions of the beam compared with the time to failure of the Random excitation tests. It was ruled out that the only initial condition fully controllable by human interaction, the initial length of the notch, was the factor at play. All specimens were measured and the notch length was relatively well controlled. This leaves the initial conditions of the specimen as the apparent major contributor to the fatigue initiation. It is also possible

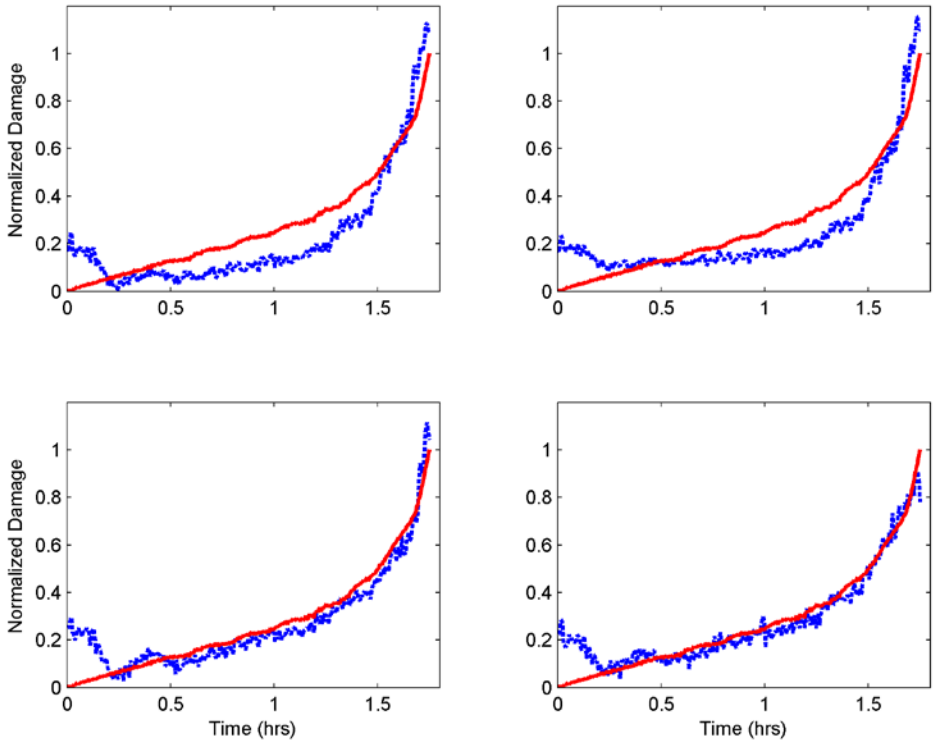

Figure 25. Smooth trends (dashed blue) projected onto the ACPD signal (solid red). Top left: first smooth trend; Top right: first two smooth trends; Bottom left: first three smooth trends; Bottom right: first four smooth trends.

that the Random excitation is much more effective at consistently initiating stage II constant fatigue crack growth.

A very important problem to address is to decipher from the extracted smooth trends which characteristics can be directly attributed to fatigue crack growth and not some other slow process. It is evident by examining the dominant smooth trend, that the fatigue is tracked well close to the end of the experiment. This makes sense, because fatigue will dominate the system at this point in the experiment. However, as pointed out previously, there is often an anomaly present in the beginning of the trend. It will be very interesting to determine whether this anomaly is due to something such as deformation of the beam from the equilibrium position, or fatigue directly. It is also

possible that the fatigue can be better tracked by looking at projections of more than one of the smooth trends. For example, by projecting the two smoothest trends onto the ACPD signal in the least squares sense, the resulting trend follows the fatigue in much better correspondence, especially in the constant crack growth region. This result is shown in Figure 23 where the ACPD signal, the first smooth trend and the linear combination of the first two, three and four smooth trends are shown.

Chapter 5

CONCLUSION

A novel fatigue testing apparatus was designed, built and tested at the University of Rhode Island's nonlinear dynamics laboratory. The new design has numerous advantages over the commercially available machines as well as other novel apparatuses. Mainly: 1) the ability to duplicate arbitrary load histories, 2) the ability to conduct tests with different R ratios, and 3) the ability to apply high frequency loads. It is specifically designed to investigate the interplay between structural dynamics and fatigue life. The system identification procedures used successfully characterized the system and numerical model for the system has been generated. Further analysis focused on the quantification of nonlinearity in the system.

The system was tested to explore its boundaries and capabilities, while appropriate design modifications were made. The system is capable of extended length testing (maximum actual fatigue test length on the order of four days currently), facilitating very accurate specimen set up, and repeatable test results. The system is also very adaptable to modifications and changes in specimen geometry. On all counts the system is capable of being a test platform for the study of a sophisticated fatigue life estimation model.

Initial fatigue experiments have also proven the capabilities of the PSW and SOD algorithms to track parameter drift in systems driven by diverse excitations. There are characteristics evident within these trends which may prove useful for warning signs

of impending fatigue failure. Also, the hypothesis that time history, and not only probability distribution, is crucial to the fatigue accumulation was proven through experimental tests. It was also shown that linear damage laws are largely inaccurate for the estimation of fatigue life, more clearly defining the need for much more sophisticated fatigue evolution models.

5.1 Future Work

The investigation of the effects of random or chaotic excitation signals is very interesting to the author. It is the recommendation that the relationship between stress cycle distribution and fatigue life be examined more closely. Also, the signal number could be increased; for example multiple surrogate data sets could be generated and compared, multiple chaotic sets with varied parameters from the same system, or time series from different chaotic systems would be interesting to investigate.

Also, a modification of the mechanical system on the slot side of the specimen would be helpful. The ball bearing set screw method seems to work, but may not be an ideal solution. Some type of compliant mechanism could be manufactured to eliminate the issue of clearance between the slot and pin.

APPENDIX A

SPECIMEN DRAWING

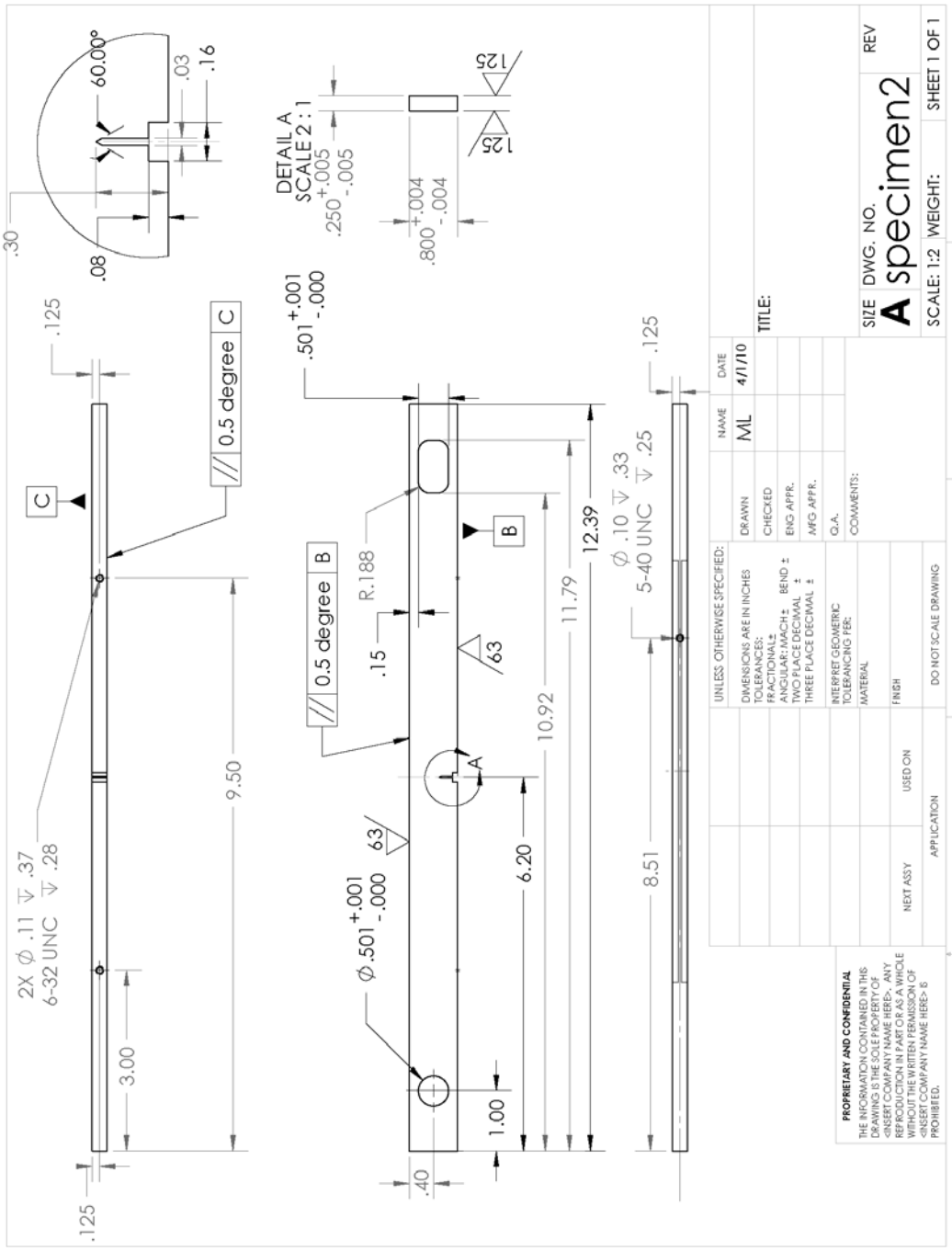

APPENDIX B

SYSTEM DRAWINGS

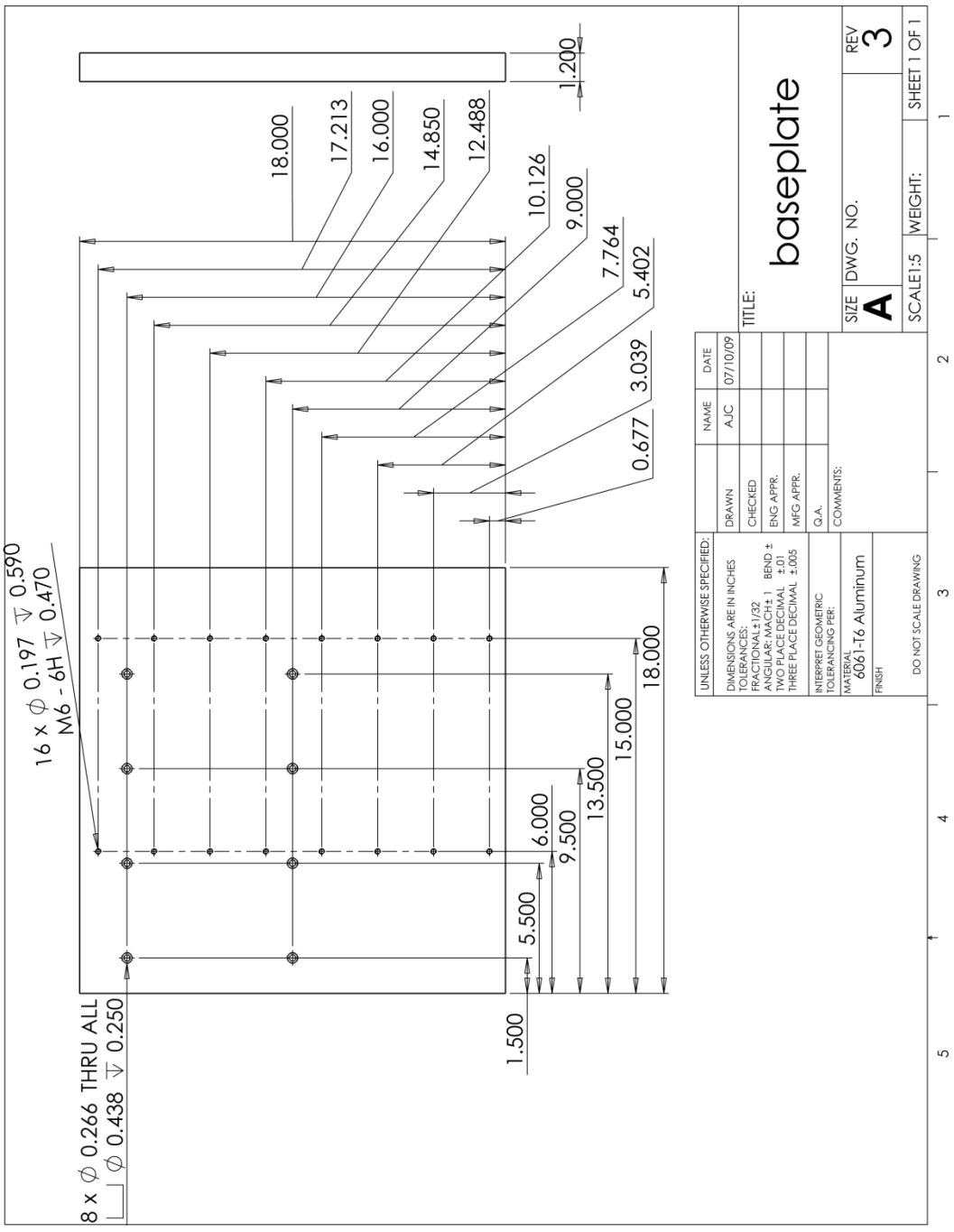

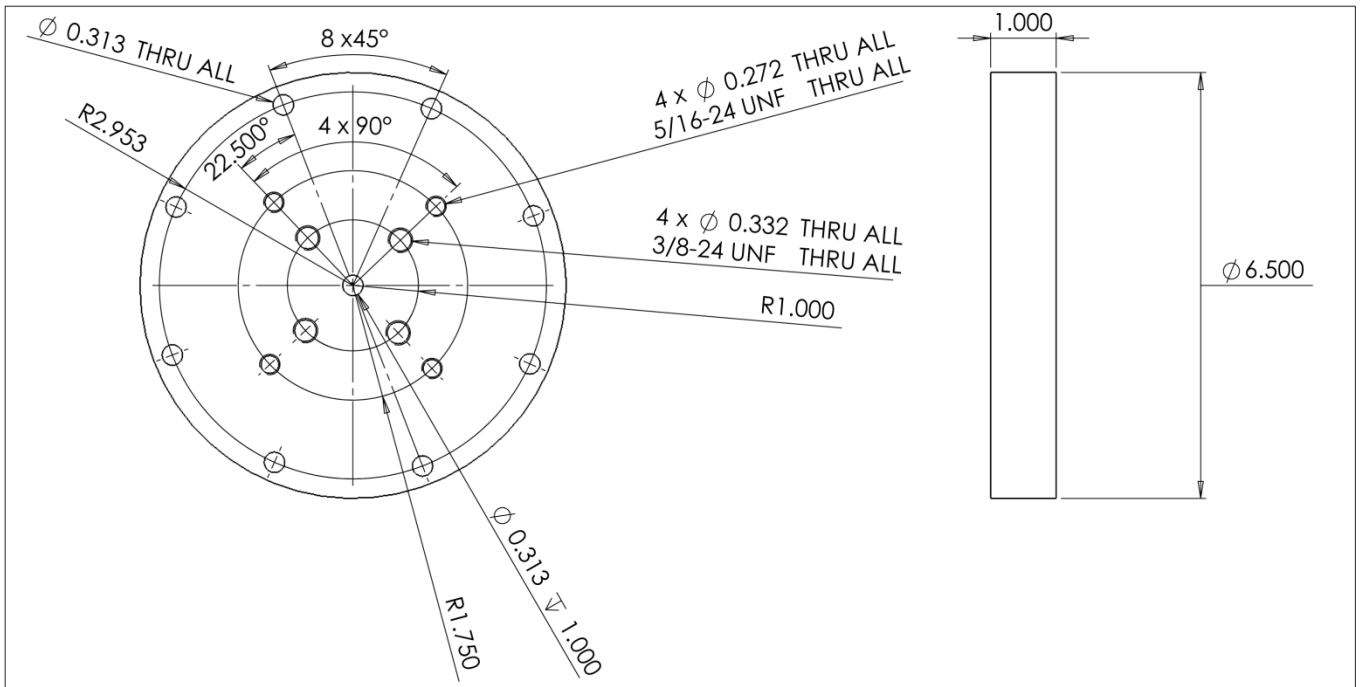

		NAME	DATE
UNLESS OTHERWISE SPECIFIED:	DRAWN	AJC	07/10/09
DIMENSIONS ARE IN INCHES TOLERANCES: FRACTIONAL ± 1/32 ANGULAR: MACH ±1 BEND ± TWO PLACE DECIMAL ±.01 THREE PLACE DECIMAL ±.005	CHECKED		
	ENG APPR.		
	MFG APPR.		
INTERPRET GEOMETRIC TOLERANCING PER:	Q.A.		
MATERIAL 6061-T6 Aluminum	COMMENTS:		
FINISH			
DO NOT SCALE DRAWING			

TITLE: bases

SIZE	DWG. NO.	REV
A		2
SCALE: 1:2	WEIGHT:	SHEET 1 OF 1

5 4 3 2 1

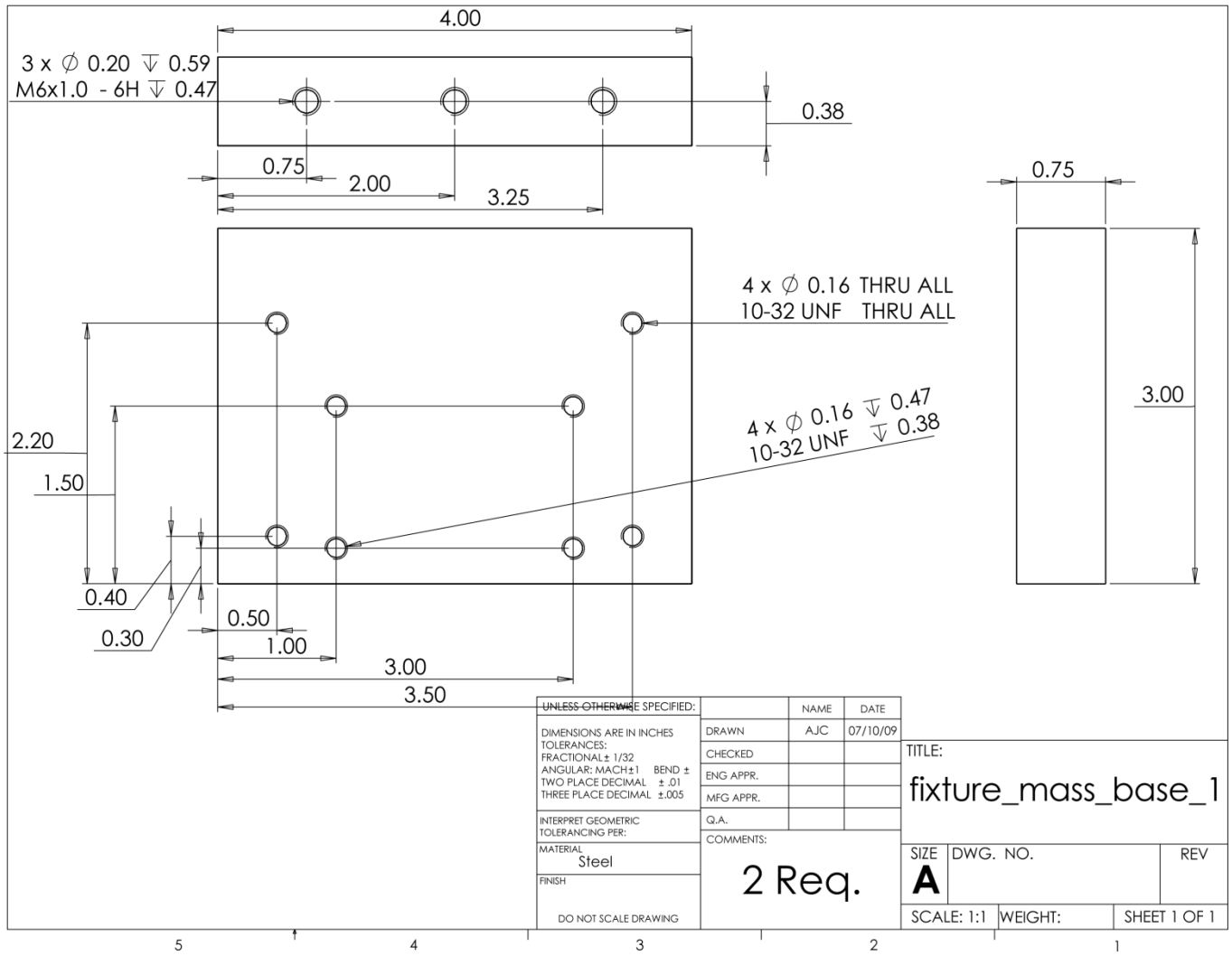
4.00
3 x ∅ 0.20 ↧ 0.59
M6x1.0 - 6H ↧ 0.47
0.38
0.75
2.00
3.25
0.75
4 x ∅ 0.16 THRU ALL
10-32 UNF THRU ALL
3.00
4 x ∅ 0.16 ↧ 0.47
10-32 UNF ↧ 0.38
2.20
1.50
0.40
0.30
0.50
1.00
3.00
3.50
UNLESS OTHERWISE SPECIFIED:
DIMENSIONS ARE IN INCHES
TOLERANCES:
FRACTIONAL ± 1/32
ANGULAR: MACH ±1 BEND ±
TWO PLACE DECIMAL ± .01
THREE PLACE DECIMAL ±.005
INTERPRET GEOMETRIC TOLERANCING PER:
MATERIAL
Steel
FINISH
DO NOT SCALE DRAWING
NAME
DATE
DRAWN
AJC
07/10/09
CHECKED
ENG APPR.
MFG APPR.
Q.A.
COMMENTS:
2 Req.
TITLE:
fixture_mass_base_1
SIZE
A
DWG. NO.
REV
SCALE: 1:1
WEIGHT:
SHEET 1 OF 1
5
4
3
2
1

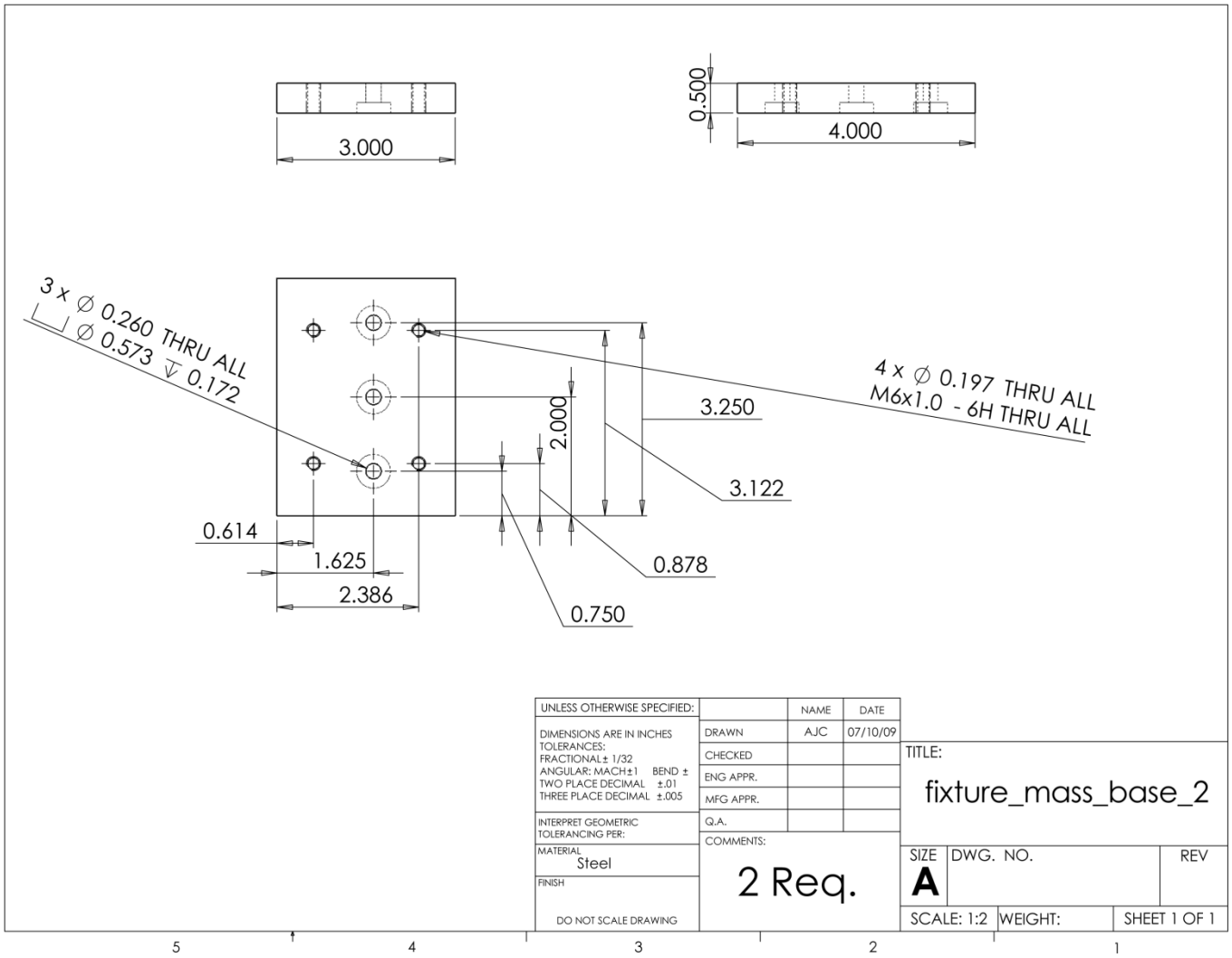
3.000
0.500
4.000
3 x ∅ 0.260 THRU ALL
⌴ ∅ 0.573 ↧ 0.172
4 x ∅ 0.197 THRU ALL
M6x1.0 - 6H THRU ALL
2.000
3.250
3.122
0.614
1.625
2.386
0.878
0.750
UNLESS OTHERWISE SPECIFIED:
DIMENSIONS ARE IN INCHES
TOLERANCES:
FRACTIONAL ± 1/32
ANGULAR: MACH ±1 BEND ±
TWO PLACE DECIMAL ±.01
THREE PLACE DECIMAL ±.005
INTERPRET GEOMETRIC TOLERANCING PER:
MATERIAL
Steel
FINISH
DO NOT SCALE DRAWING
NAME
DATE
DRAWN
AJC
07/10/09
CHECKED
ENG APPR.
MFG APPR.
Q.A.
COMMENTS:
2 Req.
TITLE:
fixture_mass_base_2
SIZE
A
DWG. NO.
REV
SCALE: 1:2
WEIGHT:
SHEET 1 OF 1
5
4
3
2
1

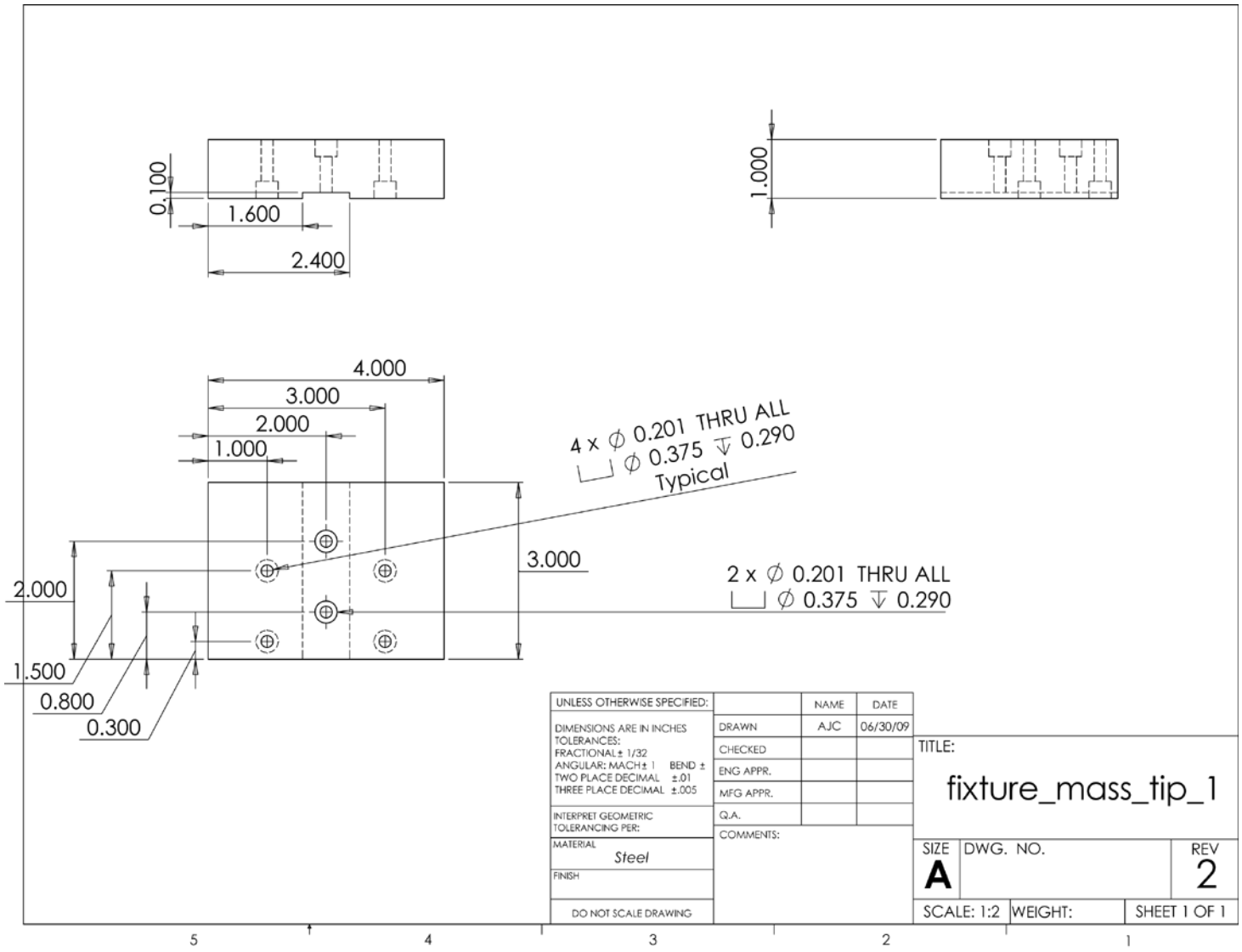
0.100
1.600
2.400
1.000
4.000
3.000
2.000
1.000
4 x ∅ 0.201 THRU ALL
⌴ ∅ 0.375 ↧ 0.290
Typical
3.000
2 x ∅ 0.201 THRU ALL
⌴ ∅ 0.375 ↧ 0.290
2.000
1.500
0.800
0.300
UNLESS OTHERWISE SPECIFIED:
DIMENSIONS ARE IN INCHES
TOLERANCES:
FRACTIONAL ± 1/32
ANGULAR: MACH ± 1 BEND ± .01
TWO PLACE DECIMAL ±.01
THREE PLACE DECIMAL ±.005
INTERPRET GEOMETRIC TOLERANCING PER:
MATERIAL
Steel
FINISH
DO NOT SCALE DRAWING
NAME
DATE
DRAWN
AJC
06/30/09
CHECKED
ENG APPR.
MFG APPR.
Q.A.
COMMENTS:
TITLE:
fixture_mass_tip_1
SIZE
A
DWG. NO.
REV
2
SCALE: 1:2
WEIGHT:
SHEET 1 OF 1
5
4
3
2
1

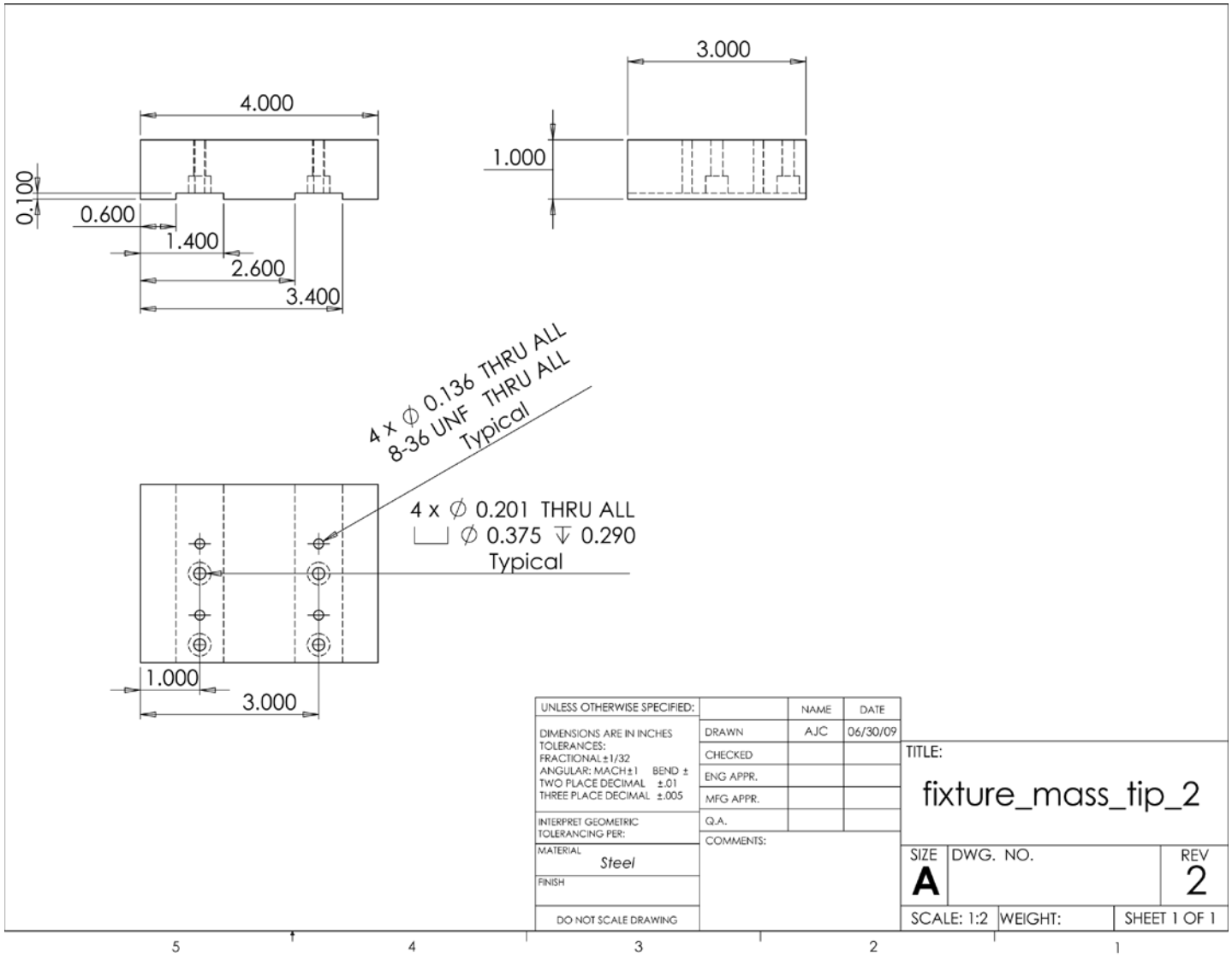
3.000
4.000
1.000
0.100
0.600
1.400
2.600
3.400
4 x ∅ 0.136 THRU ALL
8-36 UNF THRU ALL
Typical
4 x ∅ 0.201 THRU ALL
⌴ ∅ 0.375 ↧ 0.290
Typical
1.000
3.000
UNLESS OTHERWISE SPECIFIED:
DIMENSIONS ARE IN INCHES
TOLERANCES:
FRACTIONAL ±1/32
ANGULAR: MACH ±1 BEND ±
TWO PLACE DECIMAL ±.01
THREE PLACE DECIMAL ±.005
INTERPRET GEOMETRIC TOLERANCING PER:
MATERIAL
Steel
FINISH
DO NOT SCALE DRAWING
NAME
DATE
DRAWN
AJC
06/30/09
CHECKED
ENG APPR.
MFG APPR.
Q.A.
COMMENTS:
TITLE:
fixture_mass_tip_2
SIZE
A
DWG. NO.
REV
2
SCALE: 1:2
WEIGHT:
SHEET 1 OF 1
5
4
3
2
1

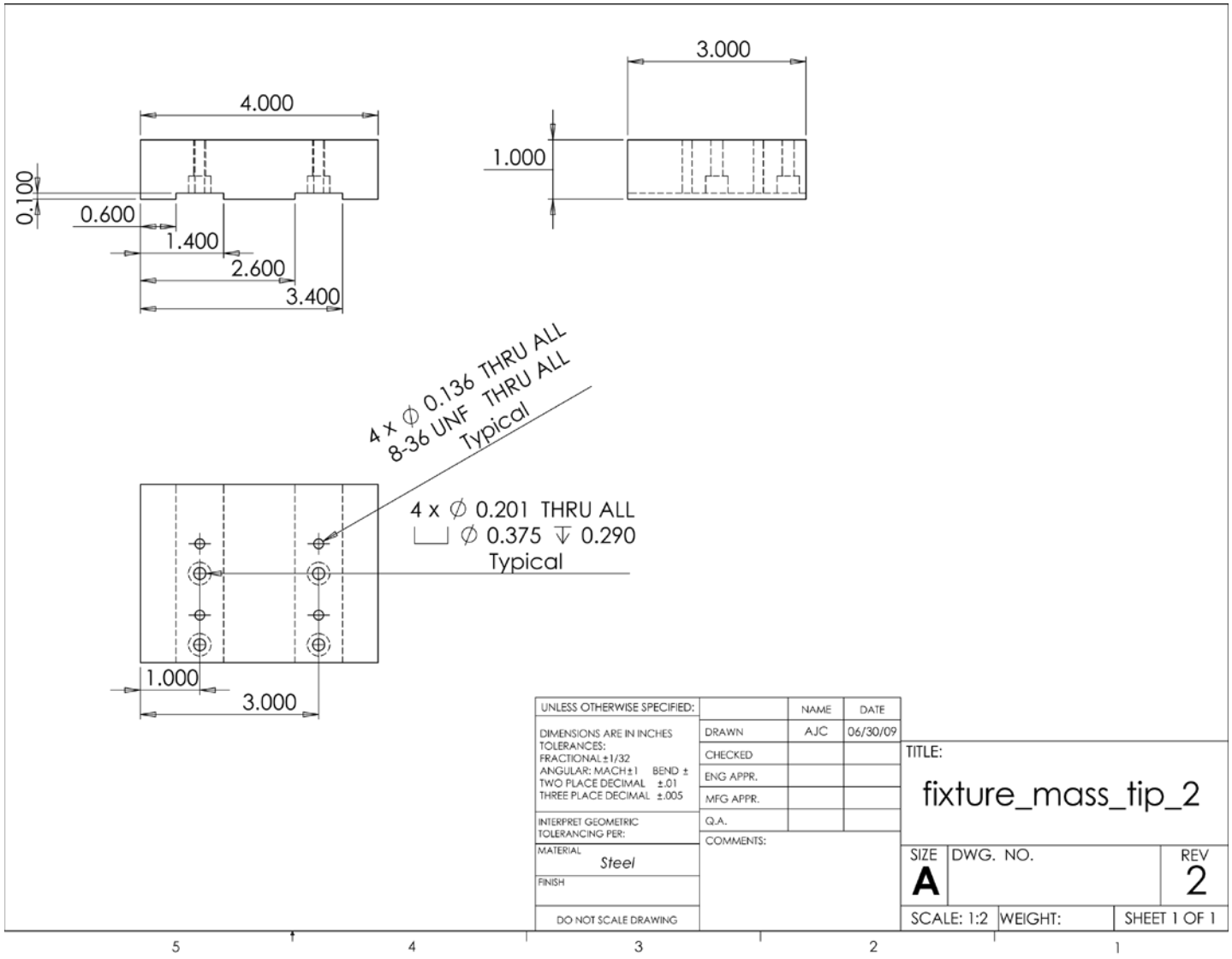
3.000
4.000
1.000
0.100
0.600
1.400
2.600
3.400
4 x ∅ 0.136 THRU ALL
8-36 UNF THRU ALL
Typical
4 x ∅ 0.201 THRU ALL
⌴ ∅ 0.375 ↧ 0.290
Typical
1.000
3.000
UNLESS OTHERWISE SPECIFIED:
DIMENSIONS ARE IN INCHES
TOLERANCES:
FRACTIONAL ±1/32
ANGULAR: MACH ±1 BEND ±
TWO PLACE DECIMAL ±.01
THREE PLACE DECIMAL ±.005
INTERPRET GEOMETRIC TOLERANCING PER:
MATERIAL
Steel
FINISH
DO NOT SCALE DRAWING
NAME
DATE
DRAWN
AJC
06/30/09
CHECKED
ENG APPR.
MFG APPR.
Q.A.
COMMENTS:
TITLE:
fixture_mass_tip_2
SIZE
A
DWG. NO.
REV
2
SCALE: 1:2
WEIGHT:
SHEET 1 OF 1
5
4
3
2
1

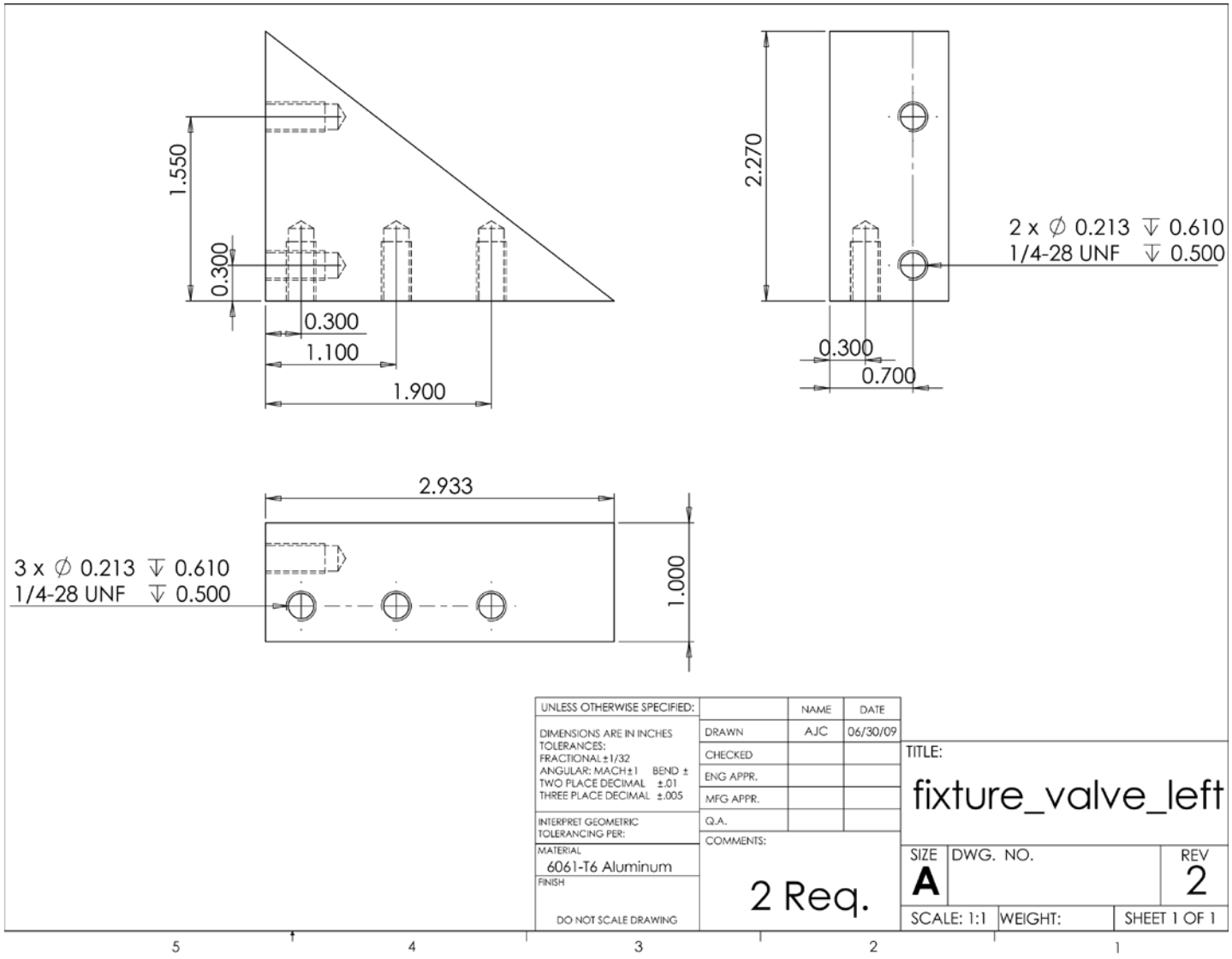
1.550
0.300
0.300
1.100
1.900
2.270
2 x ∅ 0.213 ↧ 0.610
1/4-28 UNF ↧ 0.500
0.300
0.700
2.933
3 x ∅ 0.213 ↧ 0.610
1/4-28 UNF ↧ 0.500
1.000
UNLESS OTHERWISE SPECIFIED:
DIMENSIONS ARE IN INCHES
TOLERANCES:
FRACTIONAL ±1/32
ANGULAR: MACH ±1 BEND ±
TWO PLACE DECIMAL ±.01
THREE PLACE DECIMAL ±.005
INTERPRET GEOMETRIC TOLERANCING PER:
MATERIAL
6061-T6 Aluminum
FINISH
DO NOT SCALE DRAWING
NAME
DATE
DRAWN
AJC
06/30/09
CHECKED
ENG APPR.
MFG APPR.
Q.A.
COMMENTS:
2 Req.
TITLE:
fixture_valve_left
SIZE
A
DWG. NO.
REV
2
SCALE: 1:1
WEIGHT:
SHEET 1 OF 1
5
4
3
2
1

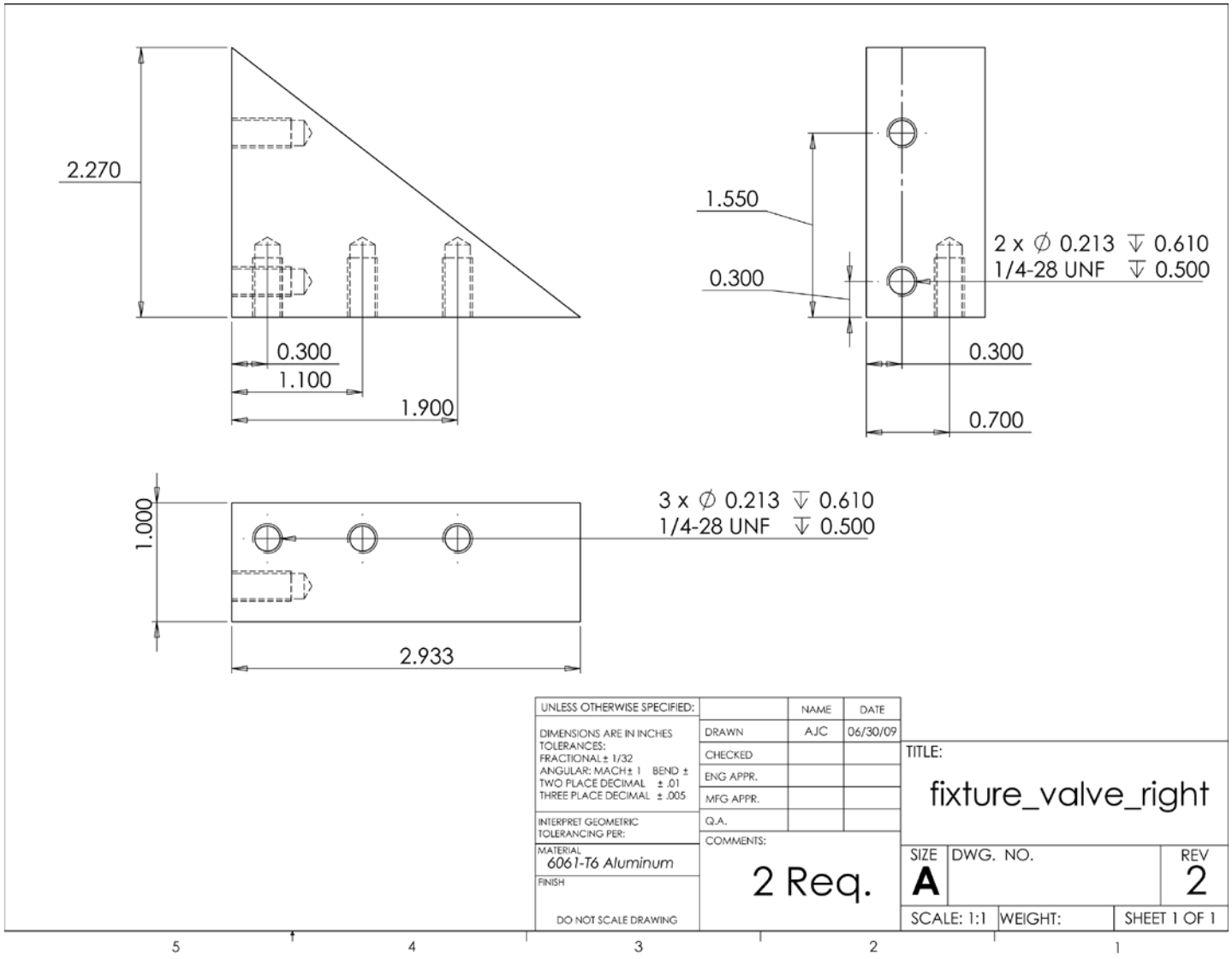
2.270
0.300
1.100
1.900
1.550
0.300
2 x ∅ 0.213 ↧ 0.610
1/4-28 UNF ↧ 0.500
0.300
0.700
1.000
3 x ∅ 0.213 ↧ 0.610
1/4-28 UNF ↧ 0.500
2.933
UNLESS OTHERWISE SPECIFIED:
DIMENSIONS ARE IN INCHES
TOLERANCES:
FRACTIONAL ± 1/32
ANGULAR: MACH ± 1 BEND ±
TWO PLACE DECIMAL ± .01
THREE PLACE DECIMAL ± .005
INTERPRET GEOMETRIC TOLERANCING PER:
MATERIAL
6061-T6 Aluminum
FINISH
DO NOT SCALE DRAWING
NAME
DATE
DRAWN
AJC
06/30/09
CHECKED
ENG APPR.
MFG APPR.
Q.A.
COMMENTS:
2 Req.
TITLE:
fixture_valve_right
SIZE
A
DWG. NO.
REV
2
SCALE: 1:1
WEIGHT:
SHEET 1 OF 1
5
4
3
2
1

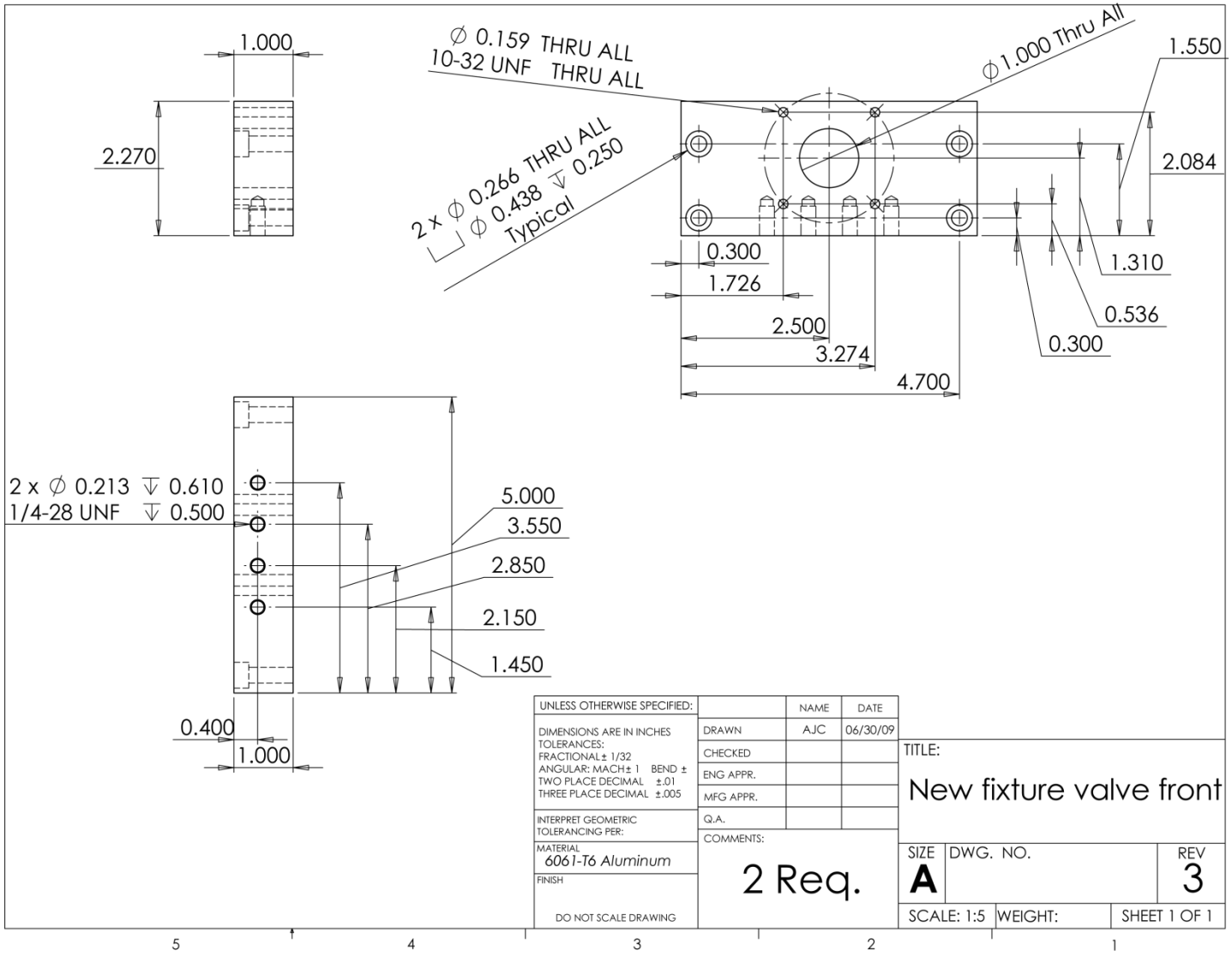
1.000
2.270
∅ 0.159 THRU ALL
10-32 UNF THRU ALL
2 x ∅ 0.266 THRU ALL
⌴ ∅ 0.438 ↧ 0.250
Typical
⌽1.000 Thru All
1.550
2.084
0.300
1.726
2.500
3.274
4.700
1.310
0.536
0.300
2 x ∅ 0.213 ↧ 0.610
1/4-28 UNF ↧ 0.500
5.000
3.550
2.850
2.150
1.450
0.400
1.000
UNLESS OTHERWISE SPECIFIED:
DIMENSIONS ARE IN INCHES
TOLERANCES:
FRACTIONAL ± 1/32
ANGULAR: MACH ± 1 BEND ±
TWO PLACE DECIMAL ±.01
THREE PLACE DECIMAL ±.005
INTERPRET GEOMETRIC TOLERANCING PER:
MATERIAL
6061-T6 Aluminum
FINISH
DO NOT SCALE DRAWING
NAME
DATE
DRAWN
AJC
06/30/09
CHECKED
ENG APPR.
MFG APPR.
Q.A.
COMMENTS:
2 Req.
TITLE:
New fixture valve front
SIZE
A
DWG. NO.
REV
3
SCALE: 1:5
WEIGHT:
SHEET 1 OF 1
5
4
3
2
1

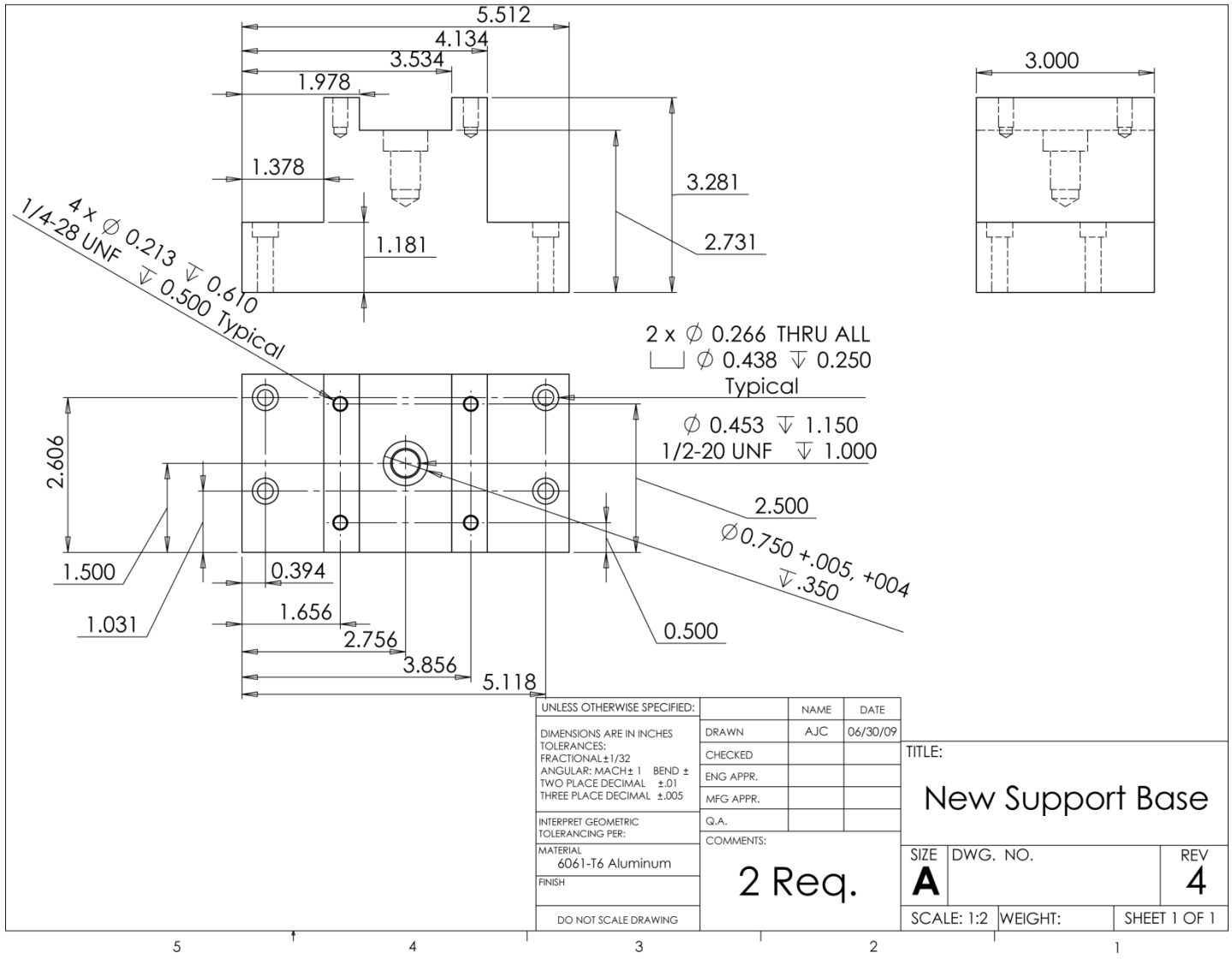
5.512
4.134
3.534
1.978
1.378
1.181
3.281
2.731
3.000
4 x ∅ 0.213 ↧ 0.610
1/4-28 UNF ↧ 0.500 Typical
2 x ∅ 0.266 THRU ALL
⌴ ∅ 0.438 ↧ 0.250
Typical
∅ 0.453 ↧ 1.150
1/2-20 UNF ↧ 1.000
2.606
2.500
∅0.750 +.005, +004
↧.350
1.500
0.394
1.031
1.656
2.756
3.856
5.118
0.500
UNLESS OTHERWISE SPECIFIED:
DIMENSIONS ARE IN INCHES
TOLERANCES:
FRACTIONAL ±1/32
ANGULAR: MACH ± 1 BEND ±
TWO PLACE DECIMAL ±.01
THREE PLACE DECIMAL ±.005
INTERPRET GEOMETRIC TOLERANCING PER:
MATERIAL
6061-T6 Aluminum
FINISH
DO NOT SCALE DRAWING
NAME
DATE
DRAWN
AJC
06/30/09
CHECKED
ENG APPR.
MFG APPR.
Q.A.
COMMENTS:
2 Req.
TITLE:
New Support Base
SIZE
A
DWG. NO.
REV
4
SCALE: 1:2
WEIGHT:
SHEET 1 OF 1
5
4
3
2
1

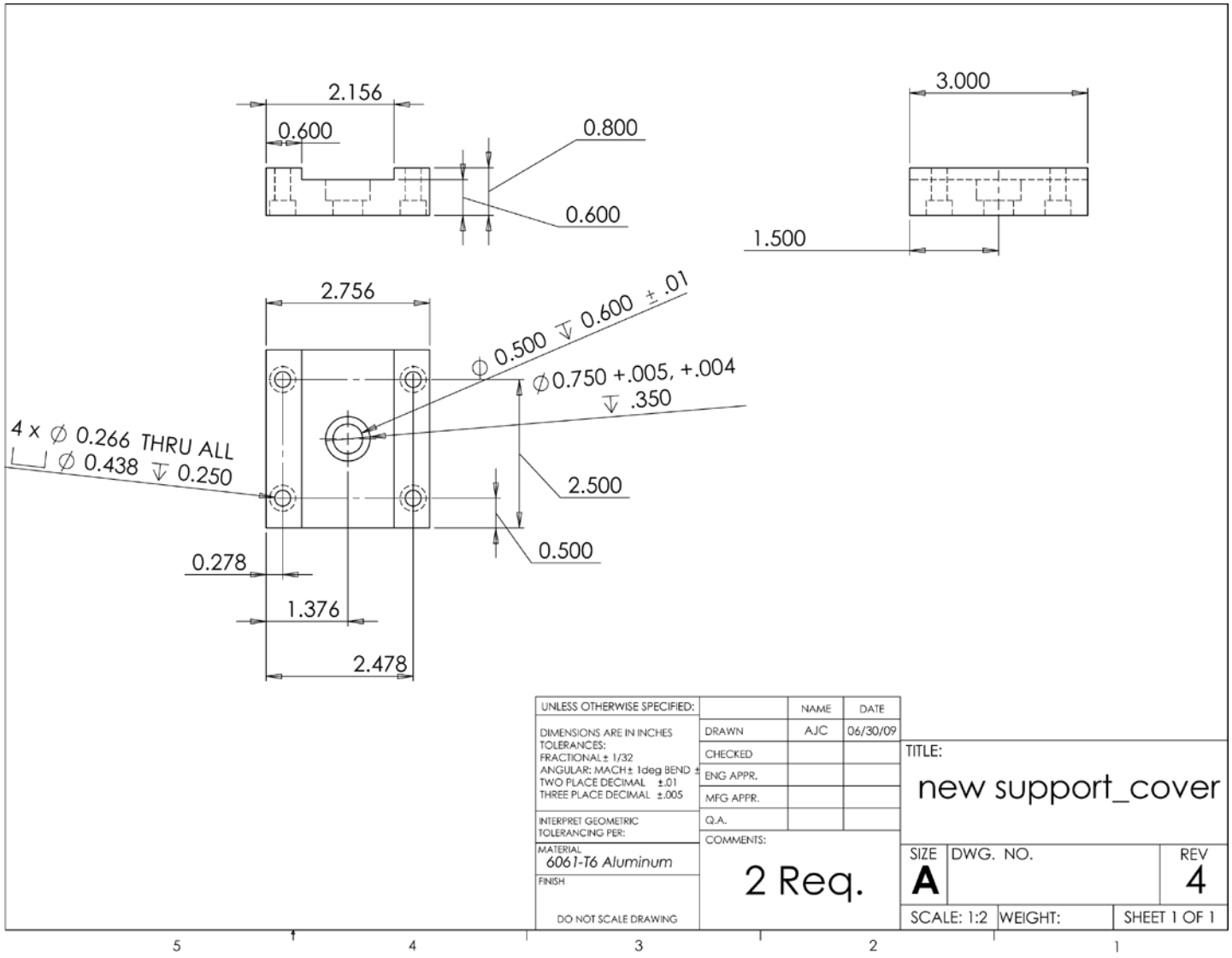
2.156
0.600
0.800
0.600
3.000
1.500
2.756
⌀ 0.500 ↧ 0.600 ± .01
⌀0.750 +.005, +.004
↧ .350
4 x ⌀ 0.266 THRU ALL
⌴ ⌀ 0.438 ↧ 0.250
2.500
0.500
0.278
1.376
2.478
UNLESS OTHERWISE SPECIFIED:
DIMENSIONS ARE IN INCHES
TOLERANCES:
FRACTIONAL ± 1/32
ANGULAR: MACH ± 1deg BEND ±
TWO PLACE DECIMAL ±.01
THREE PLACE DECIMAL ±.005
INTERPRET GEOMETRIC TOLERANCING PER:
MATERIAL
6061-T6 Aluminum
FINISH
DO NOT SCALE DRAWING
NAME
DATE
DRAWN
AJC
06/30/09
CHECKED
ENG APPR.
MFG APPR.
Q.A.
COMMENTS:
2 Req.
TITLE:
new support_cover
SIZE
A
DWG. NO.
REV
4
SCALE: 1:2
WEIGHT:
SHEET 1 OF 1
5
4
3
2
1

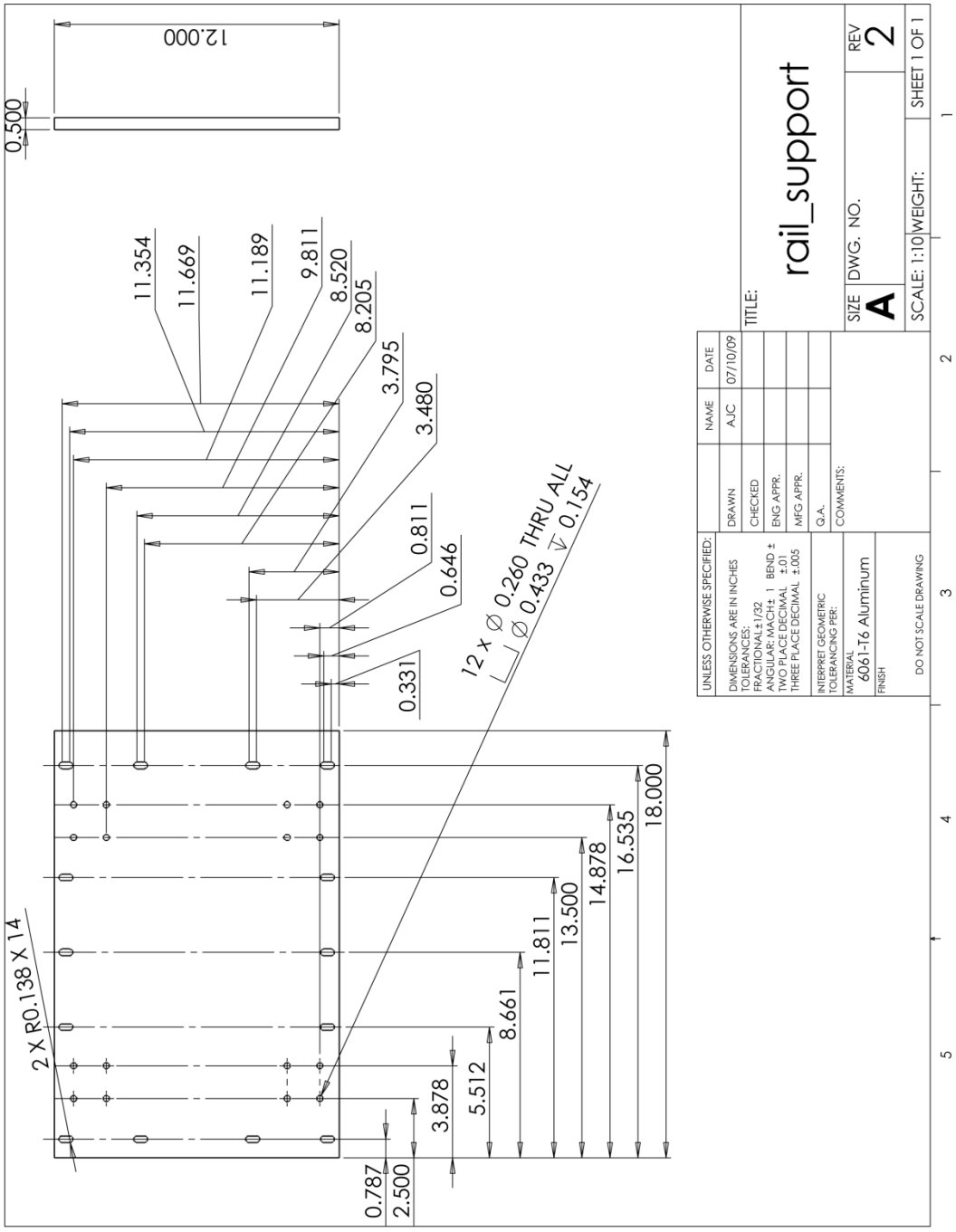
0.500
12.000
11.354
11.669
11.189
9.811
8.520
8.205
3.795
3.480
0.811
0.646
0.331
12 x Ø 0.260 THRU ALL
⌴ Ø 0.433 ↧ 0.154
2 X R0.138 X 14
18.000
16.535
14.878
13.500
11.811
8.661
5.512
3.878
2.500
0.787
UNLESS OTHERWISE SPECIFIED:
DIMENSIONS ARE IN INCHES
TOLERANCES:
FRACTIONAL ±1/32
ANGULAR: MACH ± 1 BEND ± .01
TWO PLACE DECIMAL ±.01
THREE PLACE DECIMAL ±.005
INTERPRET GEOMETRIC TOLERANCING PER:
MATERIAL 6061-T6 Aluminum
FINISH
DO NOT SCALE DRAWING
NAME
DATE
DRAWN AJC 07/10/09
CHECKED
ENG APPR.
MFG APPR.
Q.A.
COMMENTS:
TITLE:
rail_support
SIZE A
DWG. NO.
REV 2
SCALE: 1:10
WEIGHT:
SHEET 1 OF 1

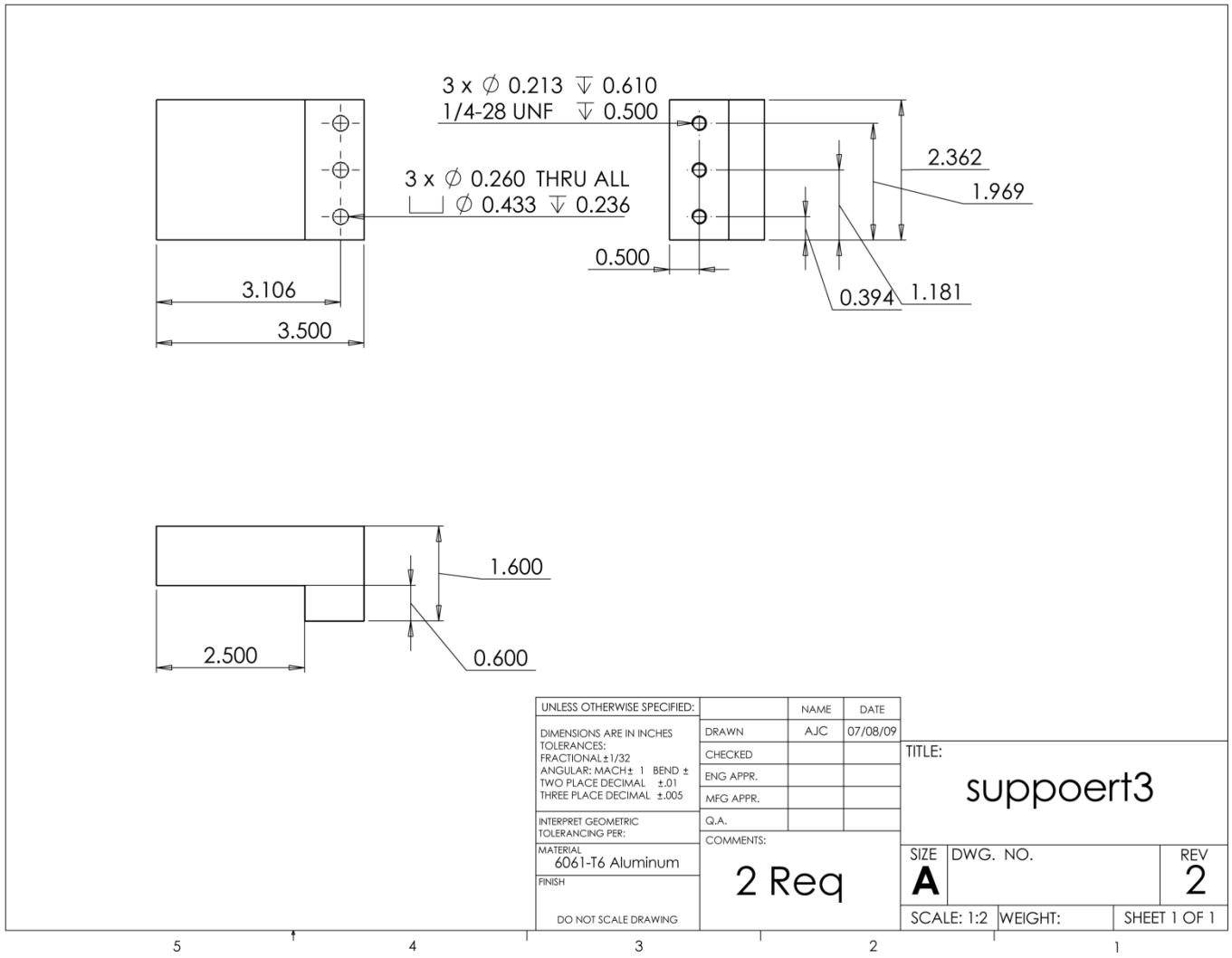
3 x ∅ 0.213 ↧ 0.610
1/4-28 UNF ↧ 0.500
3 x ∅ 0.260 THRU ALL
⌴ ∅ 0.433 ↧ 0.236
2.362
1.969
0.500
0.394
1.181
3.106
3.500
1.600
2.500
0.600
UNLESS OTHERWISE SPECIFIED:
DIMENSIONS ARE IN INCHES
TOLERANCES:
FRACTIONAL ±1/32
ANGULAR: MACH ± 1 BEND ± 1
TWO PLACE DECIMAL ±.01
THREE PLACE DECIMAL ±.005
INTERPRET GEOMETRIC TOLERANCING PER:
MATERIAL
6061-T6 Aluminum
FINISH
DO NOT SCALE DRAWING
NAME
DATE
DRAWN
AJC
07/08/09
CHECKED
ENG APPR.
MFG APPR.
Q.A.
COMMENTS:
2 Req
TITLE:
suppoert3
SIZE
A
DWG. NO.
REV
2
SCALE: 1:2
WEIGHT:
SHEET 1 OF 1
5
4
3
2
1

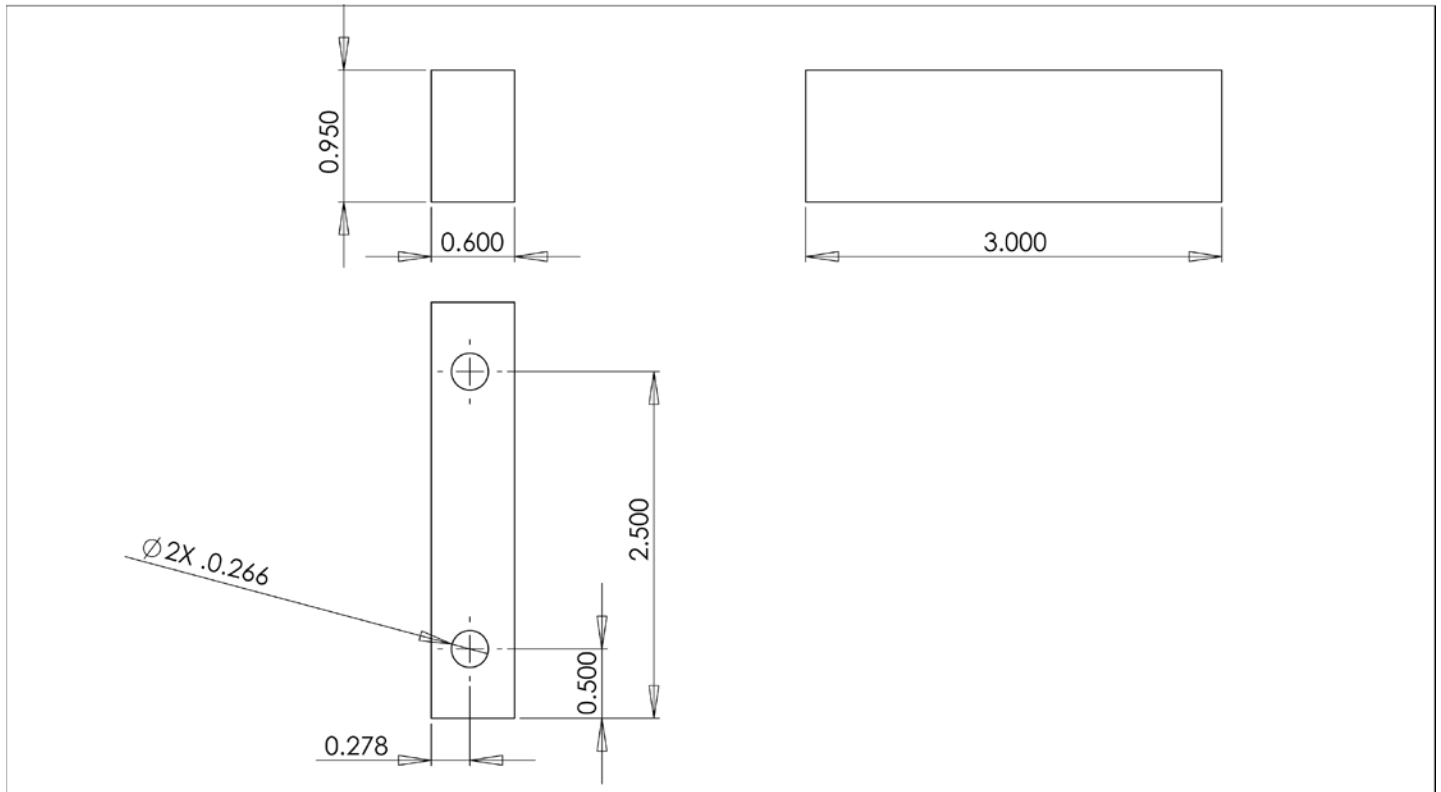

		UNLESS OTHERWISE SPECIFIED:		NAME	DATE
		DIMENSIONS ARE IN INCHES TOLERANCES: FRACTIONAL ± ANGULAR: MACH ± BEND ± TWO PLACE DECIMAL ± THREE PLACE DECIMAL ±	DRAWN		
			CHECKED		
			ENG APPR.		
			MFG APPR.		
		INTERPRET GEOMETRIC TOLERANCING PER:	Q.A.		
		MATERIAL	COMMENTS:		
NEXT ASSY	USED ON	FINISH			
APPLICATION		DO NOT SCALE DRAWING			

TITLE:

SIZE	DWG. NO.	REV
A	Support Spacer	
SCALE: 1:1	WEIGHT:	SHEET 1 OF 1

5 4 3 2 1

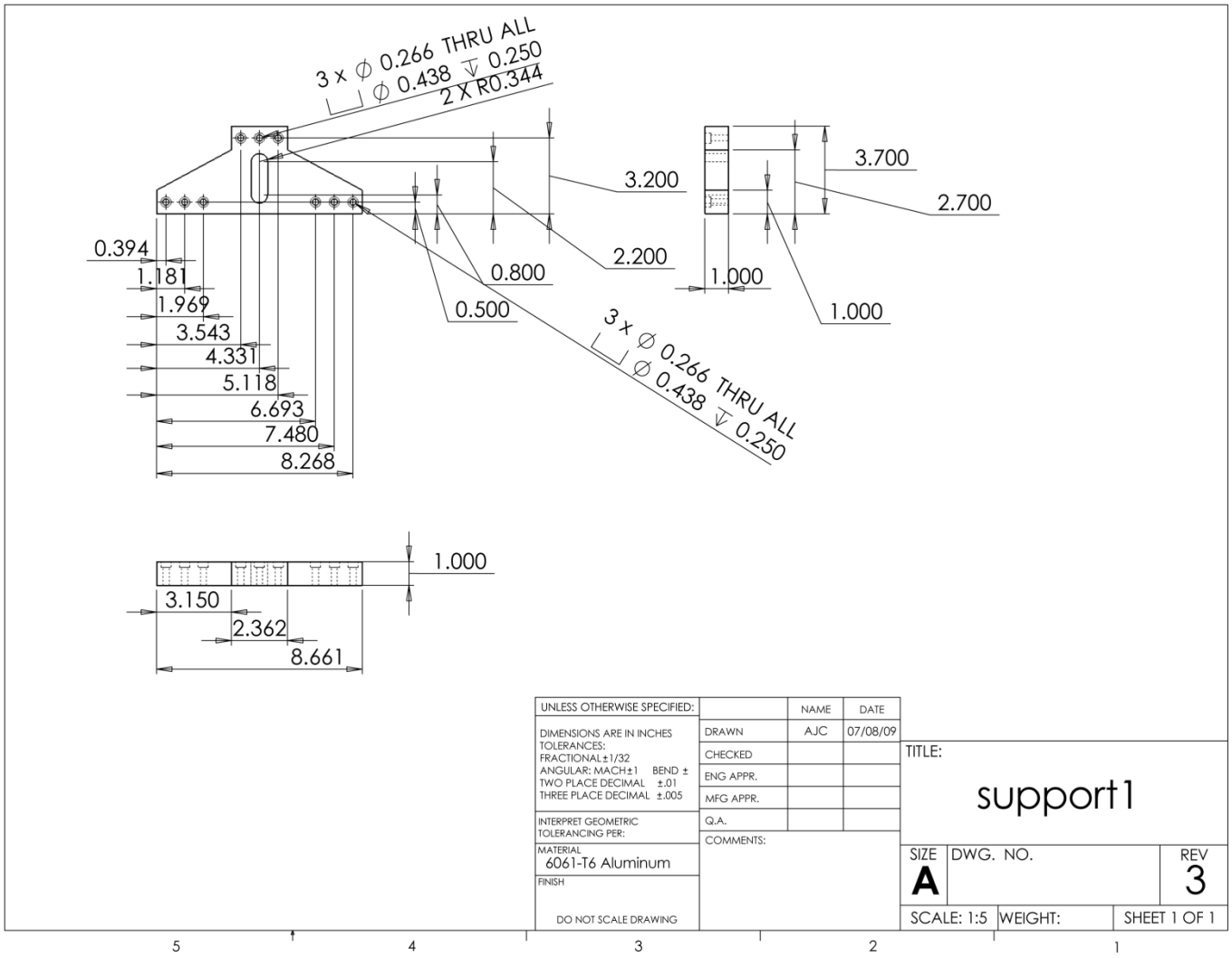
3 x ⌀ 0.266 THRU ALL
⌴ ⌀ 0.438 ↧ 0.250
2 X R0.344
3.200
2.200
0.800
0.500
3.700
2.700
1.000
1.000
0.394
1.181
1.969
3.543
4.331
5.118
6.693
7.480
8.268
3 x ⌀ 0.266 THRU ALL
⌴ ⌀ 0.438 ↧ 0.250
1.000
3.150
2.362
8.661
UNLESS OTHERWISE SPECIFIED:
DIMENSIONS ARE IN INCHES
TOLERANCES:
FRACTIONAL ±1/32
ANGULAR: MACH ±1 BEND ±
TWO PLACE DECIMAL ±.01
THREE PLACE DECIMAL ±.005
INTERPRET GEOMETRIC TOLERANCING PER:
MATERIAL
6061-T6 Aluminum
FINISH
DO NOT SCALE DRAWING
NAME
DATE
DRAWN
AJC
07/08/09
CHECKED
ENG APPR.
MFG APPR.
Q.A.
COMMENTS:
TITLE:
support1
SIZE
A
DWG. NO.
REV
3
SCALE: 1:5
WEIGHT:
SHEET 1 OF 1
5
4
3
2
1

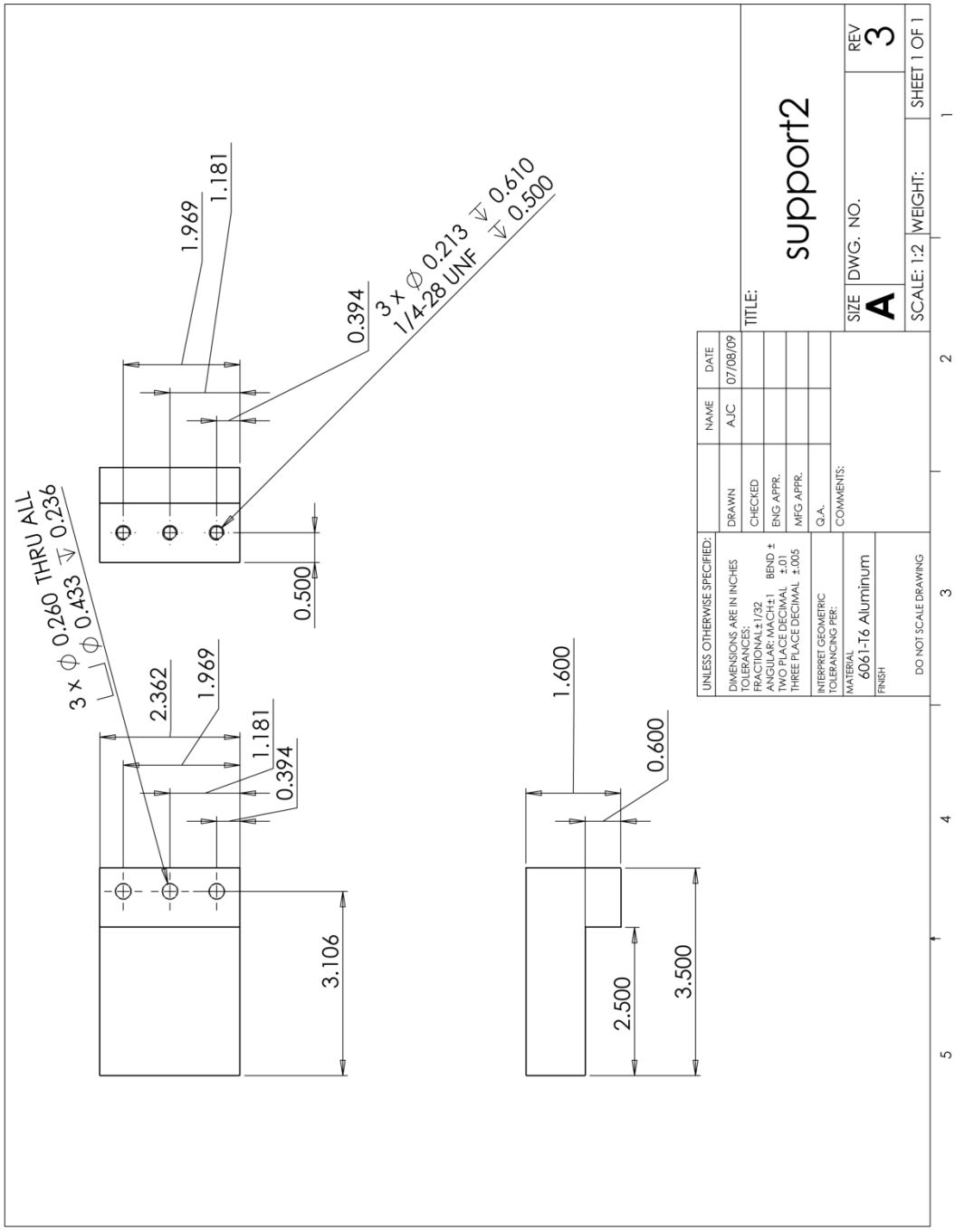
3 x Φ 0.260 THRU ALL
Φ 0.433 ↧ 0.236
2.362
1.969
1.181
0.394
3.106
1.969
1.181
0.394
3 x ∅ 0.213 ↧ 0.610
1/4-28 UNF ↧ 0.500
0.500
1.600
0.600
2.500
3.500
UNLESS OTHERWISE SPECIFIED:
DIMENSIONS ARE IN INCHES
TOLERANCES:
FRACTIONAL ± 1/32
ANGULAR: MACH ± 1 BEND ± .01
TWO PLACE DECIMAL ±.01
THREE PLACE DECIMAL ±.005
INTERPRET GEOMETRIC TOLERANCING PER:
MATERIAL
6061-T6 Aluminum
FINISH
DO NOT SCALE DRAWING
NAME
DATE
DRAWN
AJC
07/08/09
CHECKED
ENG APPR.
MFG APPR.
Q.A.
COMMENTS:
TITLE:
support2
SIZE
A
DWG. NO.
REV
3
SCALE: 1:2
WEIGHT:
SHEET 1 OF 1

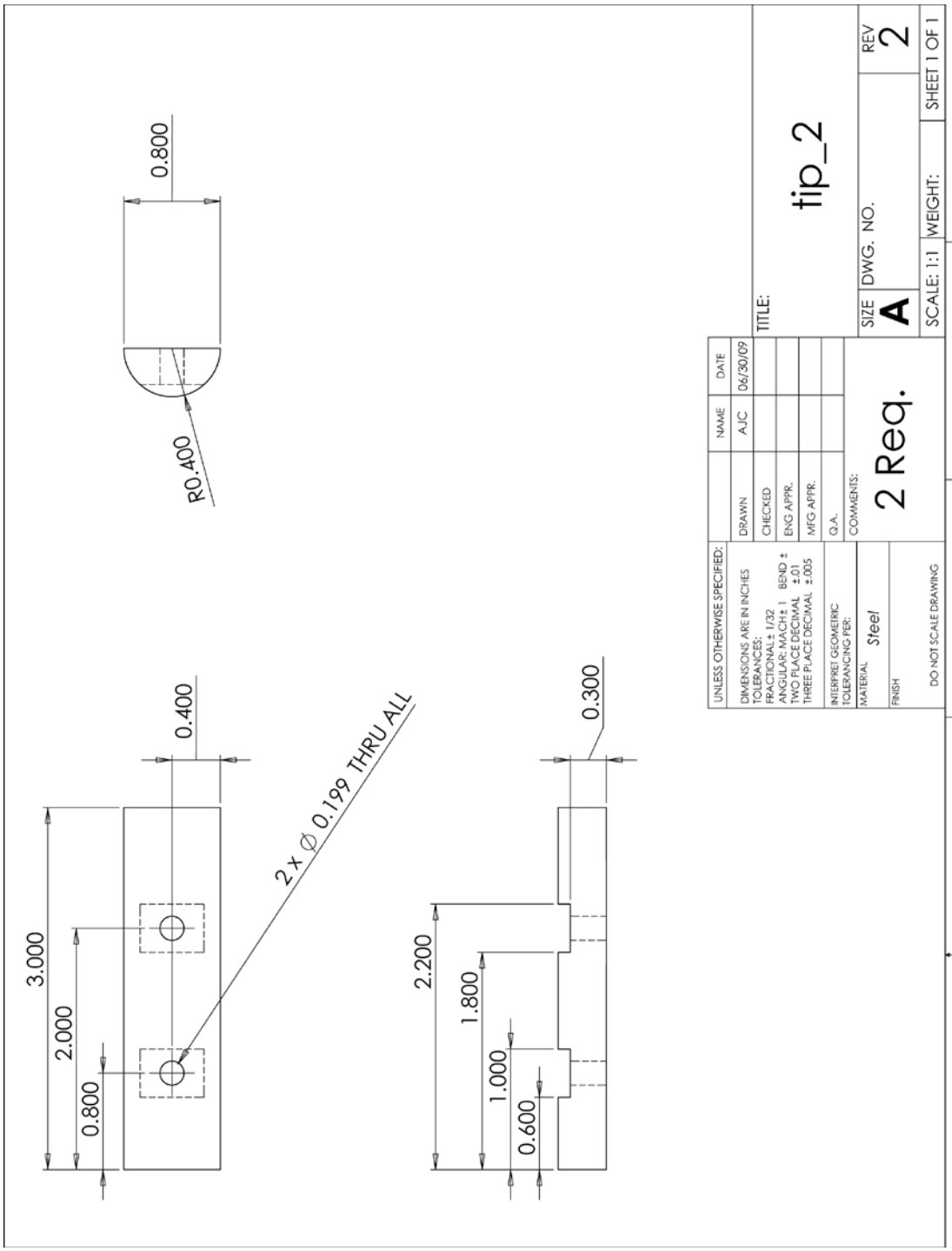
0.800
R0.400
3.000
2.000
0.800
0.400
2 x ∅ 0.199 THRU ALL
2.200
1.800
1.000
0.600
0.300
UNLESS OTHERWISE SPECIFIED:
DIMENSIONS ARE IN INCHES
TOLERANCES:
FRACTIONAL ± 1/32
ANGULAR: MACH ± 1 BEND ± .01
TWO PLACE DECIMAL ±.01
THREE PLACE DECIMAL ±.005
INTERPRET GEOMETRIC TOLERANCING PER:
MATERIAL Steel
FINISH
DO NOT SCALE DRAWING
NAME
DATE
DRAWN AJC 06/30/09
CHECKED
ENG APPR.
MFG APPR.
Q.A.
COMMENTS:
2 Req.
TITLE:
tip_2
SIZE A
DWG. NO.
REV 2
SCALE: 1:1
WEIGHT:
SHEET 1 OF 1

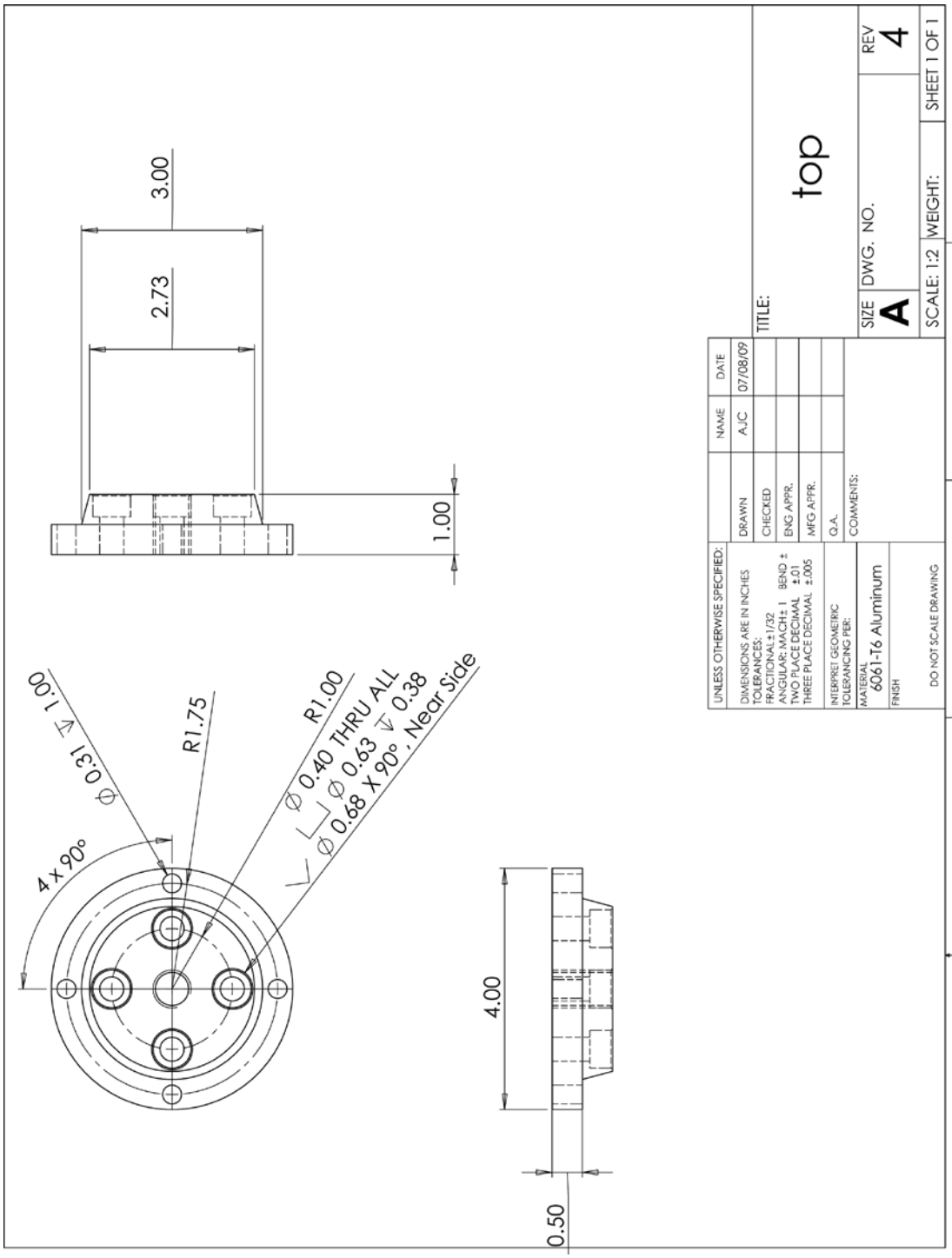
3.00
2.73
1.00
4 X 90°
R1.75
R1.00
4.00
0.50
top
UNLESS OTHERWISE SPECIFIED:
DRAWN
CHECKED
ENG APPR.
MFG APPR.
Q.A.
COMMENTS:
NAME
AJC
DATE
07/08/09
TITLE:
SIZE
A
DWG. NO.
REV
4
SCALE: 1:2
WEIGHT:
SHEET 1 OF 1
DO NOT SCALE DRAWING
MATERIAL
6061-T6 Aluminum
FINISH

BIBLIOGRAPHY

Anderson, T. L. (1995). *Fracture mechanics: fundamentals and applications.* CRC Pr I Llc.

Budynas, R. G., & Nisbett, J. K. (2008). *Shigley's mechanical engineering design* (Vol. 10). McGraw-Hill.

Chelidze, D., & Cusumano, J. P. (2004). Identifying Multideminsional Damage in a Hierarchial Dynamic System. *Nonlinear Dynamics , 37* (4), 307-322.

Chelidze, D., & Cusumano, J. P. (2006). Phase space warping: nonlinear time-series analysis for slowly drifting systems. *Phil. Trans. R. Soc. A* , 2495-2513.

Chelidze, D., & Liu, M. (2005). Dynamical Systems Approach to Fatigue Damage Identification. *Journal of Sound and Vibration , 281*, 887-904.

Chelidze, D., & Zhou, W. (2008). Smooth orthogonal decomposition for modal analysis of randomly excited systems. *Journal of Sound and Vibration , 316*, 137-146.

Chelidze, D., Cusumano, J. P., & Chatterjee, A. (2002). A dynamical systems approach to damage evolution tracking, Part 1: Description and Experimental Application. *Journal of Vibrations and Acoustics , 124* (2), 250-257.

Downing, S. D., & Socie, D. F. (1982). Simple rainflow counting algorithms. *International journal of fatigue , 4* (1), 31-40.

Farrar, C. R., Worden, K., Park, G., Todd, M., Nichols, J., Adams, D. E., et al. (2007). *Nonlinear system identification for damage detection.* Technical Report LA-14353, Los Alamos National Laboratory.

Fatemi, A., & Yang, L. (1998). Cumulative fatigue damage and life prediction theories: a survey of the state of the art for homogeneous materials. *Int. J. Fatigue , 20* (1), 9-34.

Foong, C. H., Wiercigroch, M., & Deans, W. F. (2003). An Experimental Rig to Investigate Fatigue Crack Growth Under Dynamic Loading. *Meccanica , 38* (1), 19-31.

Foong, C.-H., Wiercigroch, M., & Deans, W. F. (2006). Novel Dynamic fatigue-testing device: design and measurement. *Measurements Science and Technology* , 2218-2226.

Fraser, A., & Swinney, H. (1986). Independent coordinates for strange attractors from mutual information. *Physical Reviews A , 33* (2), 1134-1140.

Galal, & Shawki. (1990). A reeview of fatigue testing machines. *Engineering Journal of Qatar University , 3*.

Gu, M., Xu, Y. L., Chen, L. Z., & Xiang, H. F. (1999). Fatigue life estimation of steel girder of Yangpu cable-stayed bridge due to buffeting. *Jounal of Wind Engineering* , 383-400.

Hong, X., Mitchell, R. J., Chen, S., Harris, C. J., Li, K., & Irwin, G. W. (2008). Model selection approaches for nonlinear system identification: a review. *International Journal of Systems Science* , 925-946.

Jaksic, N., Foong, C.-H., Wiercigroch, M., & Boltezar, M. (2008). Parameter Identification and modelling of the fatigue-testing rig. *International Journal of Mechanical Sciences , 20*, 1142-1152.

Kantz, Holger, & Schreiber. (2004). *Nonlinear Time Series Analysis.* Cambridge: Cambridge University Press.

Kennel, M., Brown, R., & Abarbanel, H. (1992). Determining embedding dimension for phase-space reconstruction using a geometrical construction. *Physical Reviews A , 45* (6), 3403-3411.

Kerschen, G., Worden, K., Vakakis, A. F., & Golinval, J. (2006). Past, present and future of nonlinear system identification in structural dynamics. *Mechanical Systems and Signal Processing* , 505-592.

Lee, Y.-L., Pan, J., Hathaway, R., & Barkey, M. (2004). *Fatugue Testing and Analysis: Theory and Practice.* Butterworth-Heinemann.

Ljung, L. (1987). *System Identification: theory for the user.* Prentice-Hall.

Mohammad, K. S., Worden, K., & Tomlinson, G. R. (1992). Direct parameter estimation for linear and non-linear structures. *Journal of Sound and Vibration , 152* (3), 471-499.

Moon, F. C., & Holmes, P. J. (1979). A magnetoelastic strange attractor. *Journal of Sound and Vibration , 65* (2), 275-296.

Olsson, H., Astrom, K. J., Canudas de Wit, C., Gafvert, M., & Lischinsky, P. (1998). Friction models and friction compensation. *European Journal of Control* , 176-195.

Sanford, R. J. (2003). *Principles of Fracture Mechanics.* Prentice Hall.

Schreiber, T., & Schmitz, A. (1996). Improved surrogate data for nonlinearity tests. *Physical Review Letters , 77* (4), 635-638.

Sibson, R. (1985). *Manual for the TILE4 Interpolation Package.* University of Bath: Department of Mathematics and Statistics.

Smith, R., & Hillmansen, S. (2004). A brief historical overview of the fatigue of railway axles. *Proceedings of the Institution of Mechanical Engineers, Part F: Journal of Rail and Rapid Transit , 218* (4), 267-277.

Sonsino, C. M. (2007). Fatigue testing under variable amplitude loading. *Internattional Journal of Fatigue* (29), 1080-1089.

Stephens, R. I., Fatemi, A., Stephens, R. R., & Fuchs, H. O. (2000). *Metal Fatigue in Engineering.* Wiley-Interscience.

Surace, C., Worden, K., & Tomlimson, G. R. (1992). An improved nonlinear model for an automotive shock absorber. *Nonlinear Dynamics , 3*, 413-429.

Worden, K., & Tomlinson, G. R. (2001). *Nonlinearity in structural dynamics: detection, identification and modeling.* Institute of Physicd.